Cell Reports

The oxygen sensor PHD2 controls dendritic spines and synapses via modification of filamin A

--Manuscript Draft--

Manuscript Number:	CELL-REPORTS-D-15-03067R2
Full Title:	The oxygen sensor PHD2 controls dendritic spines and synapses via modification of filamin A
Article Type:	Research Article
Keywords:	prolyl hydroxylase 2; PHD2; Filamin A; dendritic spine remodeling; hypoxia, synaptic activity
Corresponding Author:	Peter Carmeliet VIB - KU Leuven Leuven, BELGIUM
First Author:	Inmaculada Segura
Order of Authors:	Inmaculada Segura
	Christian Lange
	Ellen Knevels
	Anastasiya Moskalyuk
	Rocco Pulizzi
	Guy Eelen
	Thibault Chaze
	Cicerone Tudor
	Cyril Boulegue
	Matthew Holt
	Dirk Daelemans
	Mariette Matondo
	Bart Ghesquière
	Michele Giugliano
	Carmen Ruiz de Almodovar
	Mieke Dewerchin
	Peter Carmeliet
Abstract:	Neuronal function is highly sensitive to changes in oxygen levels, but how hypoxia affects dendritic spine formation and synaptogenesis is unknown. Here, we report that hypoxia, chemical inhibition of the oxygen sensing prolyl hydroxylase domain proteins (PHDs) or silencing of Phd2 induce immature filopodia-like dendritic protrusions, promote spine regression, reduce synaptic density and decrease the frequency of spontaneous action potentials, independently of HIF-signaling. We identified the actin cross-linker filamin A (FLNA) as a novel target of PHD2 mediating these effects. In normoxia, PHD2 hydroxylates the proline residues P2309 and P2316 in FLNA, leading to von Hippel-Lindau (VHL)-mediated ubiquitination and proteasomal degradation. In hypoxia, PHD2 inactivation rapidly upregulates FLNA protein levels due to blockage of its proteasomal degradation. FLNA upregulation induces more immature spines, while Flna silencing rescues the immature spine phenotype induced by PHD2 inhibition.
Suggested Reviewers:	
Opposed Reviewers:	

Powered by Editorial Manager® and ProduXion Manager® from Aries Systems Corporation

VIB Vesalius Research Center

Dr. Sabbi Lall
Editor
Cell Reports
600 Technology Square, STE 5
Cambridge, MA 02139

Leuven, February 2, 2016

Ref.: CELL-REPORTS-D-15-03067R1

Dear Dr. Lall,
Dear Sabbi,

Thank you for your positive editorial decision about our revised manuscript entitled "The oxygen sensor PHD2 controls dendritic spines and synapses via modification of filamin A" by I. Segura *et al*., now "accepted in principle".

Please find enclosed the updated version of our manuscript, in which the text and figures were adapted to comply with the specified requirements of Cell Reports.

As requested, a completed Final File Checklist and a filled-out Journal Publishing Agreement form have been uploaded as well.

We hope that our revised manuscript meets all requirements for publication in Cell Reports and look forward to hearing your response.

Thank you very much for your consideration.

Best personal regards,

Peter Carmeliet, M.D., Ph.D.
Professor of Medicine

VIB

Vesalius Research Center

KU Leuven

Campus Gasthuisberg O&N4
Herestraat 49 box 912
3000 LEUVEN
BELGIUM
Tel.: +32 16 37 32 35
Fax: +32 16 37 25 85

www.vib.be
www.vrc-lab.be

List of changes:

No changes to the manuscript were requested by the handling editor. Text and figures were updated to comply with the specified requirements of Cell Reports.

THE OXYGEN SENSOR PHD2 CONTROLS DENDRITIC SPINES AND SYNAPSES VIA MODIFICATION OF FILAMIN A

RUNNING TITLE: Oxygen regulates dendritic spines by PHD2 and FLNA

Inmaculada Segura[1,2,11], Christian Lange[1,2,11], Ellen Knevels[1,2], Anastasiya Moskalyuk[3], Rocco Pulizzi[3], Guy Eelen[1,2], Thibault Chaze[4], Cicerone Tudor[5], Cyril Boulegue[4], Matthew Holt[5], Dirk Daelemans[6], Mariette Matondo[4], Bart Ghesquière[7], Michele Giugliano[3,8,9], Carmen Ruiz de Almodovar[1,2,10], Mieke Dewerchin[1,2] & Peter Carmeliet[1,2]

(1) Laboratory of Angiogenesis and Vascular Metabolism, Department of Oncology, University of Leuven, Leuven, B-3000, Belgium; (2) Laboratory of Angiogenesis and Vascular Metabolism, Vesalius Research Center, VIB, Leuven, B-3000, Belgium; (3) Laboratory of Theoretical Neurobiology and Neuroengineering, University of Antwerp, Wilrijk, B-2610, Belgium; (4) Proteomics Platform, Institute Pasteur, Paris, 75015, France; (5) Laboratory of Glia Biology, VIB, Leuven, B-3000, Belgium; (6) Laboratory of Virology and Chemotherapy, Rega Institute, University of Leuven, Leuven, B-3000, Belgium; (7) Metabolomics Core Facility, Vesalius Research Center, VIB, Leuven, B-3000, Belgium; (8) Neuro-Electronics Research Flanders (NERF), Leuven, B-3001, Belgium; (9) Brain Mind Institute, Swiss Federal Institute of Technology of Lausanne, Switzerland; (10) Present address: Biochemistry Center, Heidelberg University, Heidelberg, 69120, Germany.

[11]: equal contribution

Editorial correspondence: P. Carmeliet, M.D., Ph.D.
Laboratory of Angiogenesis and Neurovascular link
Vesalius Research Center
VIB, KU Leuven, Campus Gasthuisberg O&N4
Herestraat 49 - 912,
B-3000, Leuven, Belgium
tel: 32-16-37.32.02; fax: 32-16-37.25.85
e-mail: peter.carmeliet@vib-kuleuven.be

SUMMARY

Neuronal function is highly sensitive to changes in oxygen levels, but how hypoxia affects dendritic spine formation and synaptogenesis is unknown. Here, we report that hypoxia, chemical inhibition of the oxygen sensing prolyl hydroxylase domain proteins (PHDs) or silencing of *Phd2* induce immature filopodia-like dendritic protrusions, promote spine regression, reduce synaptic density and decrease the frequency of spontaneous action potentials, independently of HIF-signaling. We identified the actin cross-linker filamin A (FLNA) as a target of PHD2 mediating these effects. In normoxia, PHD2 hydroxylates the proline residues P2309 and P2316 in FLNA, leading to von Hippel-Lindau (VHL)-mediated ubiquitination and proteasomal degradation. In hypoxia, PHD2 inactivation rapidly upregulates FLNA protein levels due to blockage of its proteasomal degradation. FLNA upregulation induces more immature spines, while *Flna* silencing rescues the immature spine phenotype induced by PHD2 inhibition.

INTRODUCTION

Synaptic transmission is the main energy consuming process in the brain and requires large amounts of ATP. Since neurons generate energy primarily oxidatively, they require oxygen. Hence, when oxygen becomes limiting, there is a risk that the ATP pool becomes exhausted. We hypothesized that neurons possess adaptive mechanisms to prevent such energy crisis during hypoxia, and speculated that hypoxia might remodel dendritic spines to reduce the energy-consuming process of synaptic transmission.

The oxygen sensors prolyl hydroxylase domain-containing proteins (PHD1-3) use oxygen to hydroxylate prolines in target proteins, such as hypoxia-inducible transcription factor alpha (HIFα) (Epstein et al., 2001). Hydroxylated HIFα is ubiquitinated by the E3 ubiquitin ligase von Hippel-Lindau (VHL), triggering proteasomal degradation (Ivan et al., 2001; Jaakkola et al., 2001). In hypoxia, PHDs are inactive, and stabilized HIFα upregulates transcription of target genes (Epstein et al., 2001). PHDs also have HIF- and hydroxylation-independent functions and targets (Wong et al., 2013).

Dendritic spines are actin-rich protrusions emerging from dendrites and receiving synaptic input. They are implicated in synaptic plasticity, learning and memory (Hotulainen and Hoogenraad, 2010). Spines sprout as filopodia that search for synaptic contact, and develop into mature spines containing the postsynaptic density receiving synaptic input (Ethell and Pasquale, 2005; Hotulainen and Hoogenraad, 2010). Among actin crosslinkers, filamin A (FLNA) promotes the formation of orthogonal networks or parallel actin bundles, depending on the filamin/F-actin ratio (van der Flier and Sonnenberg, 2001). FLNA regulates dendritic morphogenesis (Zhang et al., 2014), axonal growth cone (Zheng et al., 2011) and neuronal migration (Sarkisian et al., 2006), but it is unknown if FLNA regulates spine morphology. Notably, under- and over-expression of FLNA impair neuronal migration via distinct mechanisms (Sarkisian et al., 2006; Zhang et al., 2013; Zhang et al., 2012), indicating that neurons require precise regulation of FLNA levels.

Anecdotal observations suggest that PHDs regulate actin rearrangements via an undefined mechanism. PHD2-haplodeficient endothelial cells have impaired migration and actin cytoskeleton reorganization (Mazzone et al., 2009), while PHD2-deficient HeLa cells

show altered cell migration via a HIF-independent mechanism (Vogel et al., 2010). These findings raised the question if oxygen, via PHD2, might control actin-dependent spine formation. We thus investigated the role of PHD2 in the morphogenesis and maintenance of dendritic spines and synapses in hippocampal neurons.

RESULTS

HYPOXIA AND DMOG INDUCE IMMATURE SPINES

In mouse hippocampal neurons (MHNs), dendritic spines emerge during 8-11 days *in vitro* (DIV) and progressively mature to shorter mushroom-shaped spines at 12-15 DIV, with concomitant induction of spontaneous synchronized network-wide spiking activity (Fig. S1A-E). To evaluate if physiological levels of hypoxia (which can be as low as 0.5% O_2 in the brain (Erecinska and Silver, 2001)) affect dendritic spine formation, 13 DIV MHNs were incubated overnight (o/n) in normoxia (21% O_2) or hypoxia (1% O_2). To visualize dendritic protrusions, we transfected 10 DIV MHNs with yellow (YFP) or tandem dimer tomato (tdT) fluorescent proteins. Neurons exposed to hypoxia showed reduced protrusion density and most spines were long filopodia-like protrusions without head (Fig. 1A-E). Similar effects were seen in established mature spines, when treatment started at 20 DIV (Fig. S1F-J). These alterations were not due to changes in neuronal viability (Fig. S1K-M) or oxidative stress (Fig. S1N).

Time-lapse imaging of 14 DIV YFP-labeled MHNs for 1 hr showed that in normoxia, 45% of the spines were stable in length (variations ≤0.2 µm), while the rest slightly increased or reduced their length (Fig. 1F-H). In hypoxia (0.5% O_2) most spines became longer or regressed, and only 33% kept their original length (Fig. 1F-H). Similar effects were observed upon o/n treatment of 13 DIV MHNs with the PHD inhibitor dimethyl-oxalylglycine (DMOG), which upregulates hypoxia-responsive genes and HIF-dependent luciferase reporter (Fig. S1O,P; Fig. S2A-I), without causing apoptosis or oxidative stress (Fig. S1K-N). Neurons did not suffer irreversible damage as washout of DMOG restored spine density and maturation (Fig. S2J-M'). Thus, inactivation of PHDs (by hypoxia or pharmacologic inhibition) impaired spine maturation, caused spine regression and reduced spine density, without altering viability.

HYPOXIA AND DMOG INDUCE SYNAPTIC IMPAIRMENT

To evaluate if hypoxia and DMOG altered the electrophysiological properties of neurons, we performed patch-clamp recordings. 13 or 20 DIV MHNs were incubated o/n in normoxia, hypoxia or treated with DMOG. Neither hypoxia nor DMOG altered their passive electrical membrane properties (Fig. S3A-C) or intrinsic excitability (Fig. S3D-F), as confirmed by evoking antidromic action potentials (APs) upon repeated extracellular electrical stimulation (Fig. S3G). These results show that hypoxia or DMOG did not change the ability of neurons to initiate and propagate APs upon stimulation. They did also not alter the time-course of individual APs (Fig. S3H-K). However, hypoxia and DMOG reduced the frequency of spontaneous AP firing (Fig. 2A,B; Fig. S3L), suggesting that MHNs had fewer functional synaptic connections and received less excitatory synaptic input.

We also explored if the morphological changes of dendritic protrusions were reflected by functional alterations in synaptic transmission. Hypoxia and DMOG reduced excitatory synaptic transmission at 14 and 21 DIV, as evidenced by the suppressed spontaneous synchronized network-wide spiking activity (bursts), while inhibitory synapses were unaffected since not only burst duration, but also burst frequency was reduced (Fig. 2C,D; Fig. S3M-O). Neurons recovered from hypoxia or DMOG, and restored synchronized spiking activity 24 hrs after switching back to control conditions (Fig. 2C,D; Fig. S3M-O), consistent with the morphological recovery after DMOG washout (Fig. S2J-M').

Immunostaining showed that hypoxia and DMOG reduced synaptic density, as assessed by the decreased co-localization of the presynaptic marker vGlut1 and the postsynaptic marker PSD-95 (Fig. 2E-H), or the density of the presynaptic marker synaptophysin (Fig. S3P-S). However, no differences in the abundance or (plasma membrane) localization of the AMPA receptors GluA1 and GluA2 were detected (not shown), indicating that the reduced excitatory signaling upon hypoxia or DMOG was not due to downregulation of postsynaptic AMPA receptors. Instead, the reduced synaptic

transmission upon hypoxia or DMOG results from the remodeling of dendritic spines and the decreased synaptic density.

PHD2 IS EXPRESSED IN HIPPOCAMPAL NEURONS

To define which PHDs are involved, we analyzed the expression of PHDs. *In situ* hybridization, RT-PCR and RNAseq revealed that *Phd1* (also known as *Egln2*) and *Phd2 (Egln1)*, but not *Phd3 (Egln3)*, were detected in the brain of mouse embryos or neonates (Fig. S4A-C). In adult brain, *Phd2* was detected in the hippocampus, cortical layers II-III and V, and other regions (Fig. S4A; not shown). Low *Phd1* signal was detected in the hippocampus (Fig. S4A).

We prepared PSD fractions from 2-wks old wild type (WT) mice (Cho et al., 1992). Protein enrichment was assessed by immunoblotting (IB) for PSD-95 and synaptophysin as post- and pre-synaptic markers, respectively. IB showed that PHD2 was broadly present, including in synaptosomes and PSDs (Fig. 3A). Using an antibody specific for PHD2 in immunostainings (Fig. S4D-H), PHD2 was detected in neurites and dendritic protrusions of MHNs (Fig. 3B) and rat hippocampal neurons (RHNs) (not shown), in close apposition to synaptophysin^{+} puncta, suggesting postsynaptic localization. Wide distribution was also obtained in MHNs transfected with YFP-tagged PHD2 (PHD2^{WT}YFP) (Fig. S4I).

PHD2 SILENCING IMPAIRS DENDRITIC SPINE MATURATION

To assess if PHD2 regulated spine formation, we silenced *Phd2* in MHNs. 7 DIV MHNs were co-transfected with YFP and control scrambled shRNA (scr) or *Phd2*-specific shRNA (shPhd2). At 14 DIV, *Phd2* silencing reduced dendritic protrusion density and the frequency of spines with head, while it increased protrusion length (Fig. 3C,D,G-I). Hypoxia did not further alter these parameters in *Phd2*-silenced MHNs (Fig. 3E-I). Time-lapse imaging showed that scr MHNs behaved as control and retained most spines (Fig. S4J-L; compare to Fig. S2F-I ctrl), while shPhd2 resembled DMOG-treated neurons with

lower spine density and longer spines (Fig. S4J-L). *Phd2* silencing did not alter passive and excitable electrical membrane properties, as recorded by patch-clamp, but reduced the frequency of the spontaneously fired action potentials (Fig. S5A-J). *Phd2* silencing also impaired synaptic density as revealed by the reduced number of vGlut1^{+}/PSD-95^{+} co-clusters (Fig. 3J-L) and synaptophysin^{+} clusters (Fig. S4M-Q). Silencing of *Phd1* did not affect spines (Fig. S4R-T). Thus, PHD2 regulated the formation and maintenance of spines and synapses.

LOSS OF PHD2 IMPAIRS DENDRITIC SPINE MATURATION

To confirm the shRNA results, we isolated MHNs from *Phd2$^{lox/lox}$* embryos, and transfected them at 7 DIV with the Brainbow1.0 (BBW) plasmid alone or together with a Cre recombinase (Cre) plasmid. BBW expresses red fluorescent protein (RFP) in the absence of Cre, and cyan fluorescent protein (CFP) or YFP in the presence of Cre. Compared to control RFP^{+} neurons, YFP^{+} or CFP^{+} PHD2-deficient cells had reduced protrusion density and increased protrusion length (Fig. S4U). Similar results were obtained in MNHs from mice lacking PHD2 in neurons (PHD2^{NKO}) (Fig. 3M-Q; Fig. S4V). Also, PHD2 deletion reduced the frequency and synchronicity of spontaneous bursts of APs (Fig. 3R; Fig. S5K). The phenotype of PHD2^{NKO} spines was rescued by PHD2^{WT}YFP but not by an inactive PHD2 mutant that lacks hydroxylation activity (PHD2^{MUT}YFP) (Vogel et al., 2010) (Fig. 3S; Fig. S4W-Y). Thus, PHD2-mediated hydroxylation is required to induce dendritic spine maturation.

PHD2 REGULATES DENDRITIC SPINE AND SYNAPTIC DENSITY *IN VIVO*

To evaluate the effect of *Phd2* silencing on dendritic spines *in vivo*, we performed shRNA knockdown of *Phd2* by *in utero* electroporation of the hippocampus in E15.5 embryos (Pacary et al., 2012) with a bigenic vector co-expressing the shRNA and ZsGreen1 fluorescent protein. Analysis of dendritic spines in the hippocampal CA1 region at

postnatal day 15 (P15) revealed that spine density was reduced in shPhd2 neurons *in vivo* (Fig. 3T; Fig. S6A,B).

Golgi staining showed that spine density was reduced in PHD2^{NKO} mice (Fig. S6C-E). To gain insight in the role of PHD2 in synapse formation *in vivo*, we analyzed the *stratum radiatum* of hippocampal CA1 region. Transmission electron microscopy and immunostainings revealed that PHD2^{NKO} littermates had reduced synaptic density (Fig. S6F,G) (number of synapses / 100 µm^2: 38.98 ± 0.90 for ctrl *versus* 32.95 ± 1.17 for PHD2^{NKO}; n = 3 animals; $p < 0.001$) and synaptophysin$^+$ and PSD-95$^+$ signals (Fig. S6H-M). Thus, PHD2 regulates spine morphogenesis and synaptic density *in vivo*.

HYPOXIC SPINE REMODELING OCCURS PRIOR TO HIF-MEDIATED TRANSCRIPTION

To identify the molecular mechanism via which PHD2-mediated hydroxylation regulated spine morphogenesis, we explored the involvement of HIF-1α. We evaluated the kinetics of HIF-mediated transcription after PHD-blockade by using the 9xHRE::Luciferase reporter. Luc activity was increased, but only after 20 hrs of hypoxia or DMOG, and the blocker acriflavine abolished this effect (Fig. S1P). Thus, HIF-mediated transcription occurred later than the onset of spine remodeling, suggesting a HIF-independent mechanism. Also, hypoxia still induced dendritic spine changes in HIF-1α^{NKO} MHNs (obtained by transducing MHNs from *Hif-1α$^{lox/lox}$* mice with an adenoviral Cre-vector; not shown), further indicating that spine remodeling occurred independently of HIF-1α.

FLNA IS EXPRESSED IN DENDRITIC FILOPODIA AND SPINES

We therefore considered alternative targets for PHD2 and focused on the actin cross-linker FLNA, as it interacts with VHL (Tsuchiya et al., 1996), thus providing a putative molecular link between the cytoskeleton and hypoxia. FLNA is detected in the soma and dendrites, though its localization in spines is debated (Nestor et al., 2011; Noam et al., 2012). Staining of RHNs with a specific anti-FLNA antibody (Fig. S7A,B) used in conjunction with confocal imaging confirmed that FLNA was detectable in the soma, dendrites and in

structures resembling dendritic spines, close to synaptophysin$^+$ clusters (not shown). To enhance spatial resolution of FLNA$^+$ puncta, we used high-resolution structured illumination microscopy (SIM), which showed FLNA$^+$ puncta in filopodia-like protrusions and the head of mature dendritic spines (Fig. 4A; Fig. S7C,D). The use of SIM and YFP-transfected neurons at 14 DIV, when spines are still remodeling, may explain the more prominent detection of FLNA in spines, as compared to other studies, using conventional resolution microscopy of untransfected neurons (which makes precise spine visualization more challenging) at 3-4 weeks in culture, when spines and synapses are mature and stable (Noam et al., 2012; Nwabuisi-Heath et al., 2012).

To confirm the localization of FLNA, we transfected MHNs with Turquoise2 (TQ2)-tagged FLNA (FLNA^{FL}TQ2). In normoxia, FLNA^{FL}TQ2 was detected in the somato-dendritic compartment, especially in heads of mature dendritic spines (Fig. 4B). In hypoxia, FLNA^{FL}TQ2 was more widespread in the entire neuron, including in filopodia (Fig. 4B). The C-terminus part of FLNA (FLNA^{CT}TQ2), which does not bind actin, showed widespread distribution in MHNs, independent of oxygen levels (Fig. S7E). To provide biochemical confirmation, we prepared PSD fractions. FLNA was detected in all fractions, notably in the PSDs (Fig. 4C; Fig. S7F). Exposure of mice to hypoxia (8% O_2) for 4 hrs (a procedure upregulating HIF target genes; Fig. S7G) altered FLNA levels and/or distribution (Fig. 4C; Fig. S7F). FLNA was especially increased in the non-synaptosomal membrane fraction (Fig. 4C; Fig. S7F). Thus, FLNA was detectable in dendritic spines and PSDs of neurons, and its localization and levels were influenced by hypoxia.

FLNA IS STABILIZED BY HYPOXIA, DMOG OR PHD2 KNOCKDOWN

Hypoxia and DMOG regulated FLNA levels. Time-course studies in MHNs revealed that FLNA protein levels increased already within 15 minutes (for DMOG; not shown) and remained elevated for several hours (Fig. 4D,E; Fig. S7H,I). This upregulation was independent of gene transcription or protein translation, as *Flna* transcript levels were not induced during the first 4 hrs (Fig. S7J) and treatment of hypoxic MHNs with actinomycin D

or cycloheximide did not prevent FLNA protein upregulation (Fig. 4F; Fig. S7K). However, FLNA was upregulated when normoxic MHNs were treated with the proteasomal inhibitor MG132 in a dose-dependent manner (Fig. 4F,G; Fig. S7K,L). The combination of hypoxia plus MG132 did not further elevate FLNA levels above those in hypoxia (not shown), suggesting that hypoxia and proteasomal inhibition act via the same mechanism.

We transduced MHNs with scr or shPhd2 lentiviral vectors; IB revealed that *Phd2* silencing increased FLNA levels (Fig. 4H; Fig. S7M). FLNA levels were also higher in homogenates and non-synaptosomal fractions of $PHD2^{NKO}$ brains (Fig. 4I; Fig. S7N-S). Thus, oxygenation and PHD2 regulated FLNA protein levels via a mechanism involving proteasomal degradation.

PHD2 INTERACTS WITH DOMAINS D21-D23 OF FLNA

Prompted by the similarities between the regulation of FLNA and HIF-1α by the PHD2/ proteasome axis (Epstein et al., 2001), we hypothesized that FLNA was a target of PHD2-mediated proline hydroxylation and that hydroxylated-FLNA underwent ubiquitination and proteasomal degradation. We first tested if FLNA interacted with PHD2. We co-transfected HEK293T cells with myc-tagged FLNA ($mycFLNA^{FL}$) and $PHD2^{WT}$YFP or $PHD2^{MUT}$YFP. Co-immunoprecipitation (co-IP) showed that $PHD2^{WT}$YFP and $PHD2^{MUT}$YFP interacted with $mycFLNA^{FL}$ (Fig. 5A). FLNA and PHD2 also formed a complex in brain PSDs, but not in the non-synaptic fraction (Fig. 5B; Fig. S8A).

FLNA contains an actin binding domain (ABD), 24 IgG domains (D1 to D24), and two flexible regions (hinges H1 and H2) (Stossel et al., 2001; Zhou et al., 2010). To analyze which domains of FLNA interacted with PHD2, we generated 5 myc-tagged deletion variants of FLNA lacking domains known to interact with different binding partners (Zhou et al., 2010) (Fig. 5C). Proper folding of the FLNA variants was confirmed, since $mycFLNA^{NT}$ and $mycFLNA^{D12\text{-}D20}$ mutants bound to F-actin (not shown), and $mycFLNA^{CT}$ and $mycFLNA^{H2\text{-}D24}$ mutants (comprising the D24 dimerization domain) interacted with endogenous FLNA (Fig. S8B). Co-IPs showed that $PHD2^{WT}$YFP and $PHD2^{MUT}$YFP

interacted with the deletion mutants mycFLNA^{CT} and mycFLNA$^{D21\text{-}D23}$, but not with other domains (Fig. 5C; Fig. S8C; not shown). Complex detection was enhanced when using PHD2^{MUT}YFP, suggesting that they were stabilized in absence of hydroxylation (Fig. S8C).

We confirmed the PHD2-FLNA interaction by using fluorescence lifetime imaging microscopy (FLIM) to map the fluorescence resonance energy transfer (FRET) between the donor FLNA^{CT}TQ2 and the acceptor PHD2-YFP (using YFP as control). Co-expression of FLNA^{CT}TQ2 and YFP did not change the fluorescence lifetime of the donor (Fig. 5D). In contrast, co-expression of FLNA^{CT}TQ2 and PHD2^{WT}YFP increased FRET as evidenced by the reduced TQ2 fluorescence lifetime (Fig. 5D), indicating that they formed a complex in the range of 1-10 nm. Similar results were obtained when using PHD2^{MUT}YFP (Fig. 5D). Thus, amino acid residues 2250-2508 in FLNA were necessary for FLNA-PHD2 binding, but the hydroxylation activity of PHD2 *per se* was not required.

PHD2 HYDROXYLATES PROLINE RESIDUES P2309 AND P2316 IN FLNA

Although PHDs hydroxylate prolines in HIF-1α by recognizing a LXXLAP motif, other PHD targets lack such motif (Wong et al., 2013). The mycFLNA$^{D21\text{-}D23\text{-}WT}$ fragment contains 20 prolines, but none in a LXXLAP motif (Fig. S8D). We examined the ability of each proline to interact with PHD2, by generating glutathione S-transferase (GST) fusion peptides, each containing a proline together with 6 up- and down-stream flanking residues (Song et al., 2013). GST-fusion peptides were incubated with homogenates of HEK293T cells expressing PHD2^{MUT}YFP. IB of precipitated complexes revealed that only peptides containing the prolines 2270, 2309, 2316, 2320, 2404 and 2439 interacted with PHD2 (Fig. S8E). A weaker interaction was observed with the prolines 2294 and 2312.

To analyze if PHD2 hydroxylated FLNA prolines, we used an antibody specific for hydroxylated-prolines (OH-Pro). HEK293T cells were transfected with mycFLNA^{FL} and treated with proteasomal inhibitors MG132 or lactacystin, showing that proteasome inhibition increased FLNA hydroxylation (Fig. 5E; Fig. S8F). FLNA was also hydroxylated *in vivo* and hydroxylation was reduced in rats exposed to hypoxia (8% O_2; Fig. 5F).

To identify which prolines were hydroxylated by PHD2, we transfected HEK293T cells with plasmids encoding mycFLNA$^{D21\text{-}D23\text{-}WT}$ alone or together with PHD2^{WT}YFP. Cells were treated with vehicle or MG132, and immunoprecipitated mycFLNA$^{D21\text{-}D23\text{-}WT}$ was digested for liquid chromatography-mass spectrometry (LC-MS). Basal levels of OH-Pro of mycFLNA$^{D21\text{-}D23\text{-}WT}$ were detected in transfected cells. Hydroxylation of residues P2309, P2312 and P2316 in FNEEHIP*DSP*FVVP*VASPSGDAR (P*: OH-Pro) were enhanced in double transfected cells. The probability of hydroxylation was P2316>P2309>P2312, identifying P2316 and P2309 as most probable PHD2 hydroxylation sites (Fig. 5G; Fig. S8G; not shown).

We also mutated P2309 and P2316 to alanine (mycFLNA$^{D21\text{-}D23\text{-}P2309A}$, mycFLNA$^{D21\text{-}D23\text{-}P2316A}$) and tested their binding to PHD2 and hydroxylation upon co-transfection with PHD2^{WT}YFP. Although both sequence mutants interacted with PHD2^{WT}YFP, they were less hydroxylated than mycFLNA$^{D21\text{-}D23\text{-}WT}$ (Fig. 5H; Fig. S8H). Moreover, in the presence of DMOG, hydroxylation of mycFLNA$^{D21\text{-}D23\text{-}WT}$ was reduced to levels obtained with both sequence mutants (Fig. 5H; Fig. S8H), suggesting that PHD2 contributes to FLNA hydroxylation at P2309 and P2316.

VHL REGULATES FLNA PROTEIN LEVELS

VHL ubiquitinates hydroxylated HIFα to mark it for proteasomal degradation (Ivan et al., 2001; Jaakkola et al., 2001). As FLNA interacts with VHL (Tsuchiya et al., 1996), and VHL was present in the PSDs (Fig. 4C), we explored if VHL mediated FLNA ubiquitination. We first validated the interaction between VHL and FLNA in MG132-treated HEK293T cells cotransfected with HA-tagged VHL (HA-VHL) and mycFLNA^{FL} (Fig. 6A). FLNA deletion mutants showed that VHL bound to mycFLNA^{CT} and mycFLNA$^{D21\text{-}D23\text{-}WT}$ (Fig. 6B; not shown for mycFLNA^{NT} and mycFLNA$^{D11\text{-}D20}$). The single mutants mycFLNA$^{D21\text{-}D23\text{-}P2309A}$ and mycFLNA$^{D21\text{-}D23\text{-}P2316A}$ were still able to interact with VHL, while the triple mutant P2309/2312/2316A (mycFLNA$^{D21\text{-}D23\text{-}3P\rightarrow A}$) showed a weaker interaction (Fig. 6C, S9A). Taking together, our results suggest that hydroxylation of P2309, P2316 and possibly

P2312 was required for the interaction of FLNA with VHL.

We then evaluated if *Vhl* silencing increased FLNA levels. Transduction of MHNs with lentivirus expressing scr or Vhl-specific shRNA (shVhl, reducing VHL levels by 67 ± 4%; n = 3; $p < 0.05$) showed higher FLNA protein levels in VHL-silenced neurons (Fig. 6D). To confirm that VHL regulates FLNA levels *in vivo*, we generated VHL^{NKO} mice by crossing $Vhl^{lox/lox}$ mice with *Nestin*Cre mice. As these mice are lethal at E16.5, we made brain homogenates from E14.5 control or VHL^{NKO} littermates; as expected, HIF-1α levels were increased in VHL^{NKO} embryos (Fig. 6E). Notably, FLNA levels were higher in VHL^{NKO} mice (Fig. 6E; Fig. S9B). We analyzed if VHL deficiency increased the levels of hydroxylated FLNA. Since protein abundance in E14.5 embryo brains was insufficient for IP, E14.5 VHL^{NKO} brain extracts were blotted for OH-Pro and reblotted thereafter for FLNA. This analysis showed that the increased FLNA levels were comparably hydroxylated in VHL^{NKO} mice (Fig. 6F; Fig. S9C-E), suggesting that proline-hydroxylated FLNA was stabilized in the absence of VHL *in vivo*.

VHL UBIQUITINATES FLNA

We then assessed if the interaction of hydroxylated FLNA with VHL resulted in FLNA ubiquitination. Brains from E14.5 VHL^{NKO} and control littermates were collected in the presence of MG132 and PR-619. Tandem Ubiquitin Binding Entities (TUBE) pull-down of poly-ubiquitinated proteins followed by IB showed that FLNA was ubiquitinated less in VHL^{NKO} brains (Fig. 6G; Fig. S9F).

FLNA LEVELS DETERMINE DENDRITIC SPINE MORPHOLOGY

We assessed if FLNA stabilization was responsible for the remodeling of dendritic spines to a more immature state. Since forced overexpression of full-length FLNA was toxic (not shown), we used another strategy to elevate endogenous FLNA to physiological levels. We took advantage of the observation that overexpression of $mycFLNA^{D21\text{-}D23\text{-}WT}$ increased the levels of endogenous FLNA two-fold (Fig. 4H; Fig. 7A; Fig. S7M), akin to the

effect of hypoxia, DMOG or *Phd2* silencing (Fig. 4D-F,H; Fig. 7A; Fig. S7H,I,K,M). FLNA$^{D21\text{-}D23\text{-}WT}$ elevated FLNA levels by impairing the interaction between endogenous FLNA and PHD2, as less PHD2 was co-IP'ed with mycFLNA^{FL} in the presence of GST-FLNA$^{D21\text{-}D23\text{-}WT}$ (Fig. 7B). We therefore tested whether mycFLNA$^{D21\text{-}D23\text{-}WT}$ expression, and concomitant elevated FLNA levels, impaired dendritic spine maturation. MHNs transfected with mycFLNA$^{D21\text{-}D23\text{-}WT}$ had fewer and less mature dendritic spines (Fig. 7C,D,F-H) and formed fewer synaptic contacts (Fig. 7I-L), comparable to the response to hypoxia (hypoxia *versus* mycFLNA$^{D21\text{-}D23\text{-}WT}$: $p > 0.05$ for all parameters; not shown).

As FLNA also interacts with Rac and Cdc42 which promote mature spine formation (Nakamura et al., 2011; Tashiro and Yuste, 2004), a possible dominant negative interaction of mycFLNA$^{D21\text{-}D23\text{-}WT}$ with these small GTPases might also contribute to the more immature spine phenotype of mycFLNA$^{D21\text{-}D23\text{-}WT}$ expressing neurons. To assess the specificity of this peptide in mediating the PHD2-regulated FLNA degradation, we used the mycFLNA$^{D21\text{-}D23\text{-}3P\rightarrow A}$ mutant. Notably, this mutant failed to impair spine maturation and synaptic contact formation (Fig. 7E-H; 7K-L). While we cannot formally exclude that mycFLNA$^{D21\text{-}D23\text{-}WT}$ perturbs the interaction with other binding partners of FLNA, the lack of an effect by mycFLNA$^{D21\text{-}D23\text{-}3P\rightarrow A}$ strongly suggests that the effect of mycFLNA$^{D21\text{-}D23\text{-}WT}$ on spine morphology was due to its interaction with PHD2/VHL and to FLNA degradation, rather than to non-specific dominant negative interactions with other proteins. Notably, 14 DIV MHNs of E15.5 VHL^{NKO} mice (containing higher levels of endogenous FLNA) also showed more immature dendritic spines (Fig. S9G,H).

We explored if *Flna* silencing reverted the phenotype induced by silencing *Phd2*. We co-transfected MHNs with tdT together with scr or *Flna*-specific shRNA (shFlna) alone or together with shPhd2. shFlna reduced FLNA protein levels by 59 ± 8% ($n = 3$; $p < 0.05$). Silencing of *Flna* in MHNs alone increased protrusion length without affecting the protrusion density or the number of spines with head (Fig. 7M-S). However, in *Phd2*-silenced MHNs, *Flna* silencing largely prevented the switch to a more immature spine phenotype (Fig. 7M-S). Thus, FLNA is required for the spine morphology changes induced

by PHD2 knockdown.

DISCUSSION

ADAPTATION OF DENDRITIC SPINES TO HYPOXIA

Our study shows that oxygen, via PHD2, regulates dendritic spines and synaptic transmission. PHD2 coordinates rapid reversible adaptations of spines at least in part by controlling FLNA levels. When oxygen is limiting, PHD2 is inactivated, which diminishes proteasomal degradation of FLNA, thus inducing its stabilization and accumulation in non-synaptic locations, and increasing the ratio of FLNA to F-actin. Based on reports in other cells (van der Flier and Sonnenberg, 2001), we speculate that the increased FLNA abundance results in remodeling of the actin cytoskeleton from a mesh network in mature spine heads to parallel F-actin bundles in head-less immature elongated protrusions.

Our data suggest that diminished degradation of FLNA upon PHD2 inactivation in hypoxia rearranges the actin cytoskeleton to reduce the number of dendritic spines, synapses and synaptic transmission, without affecting intrinsic electrical membrane properties. Our findings are in line with a report that chemical inhibition of PHDs or PHD2 deficiency reduce long-term potentiation (Corcoran et al., 2013). Experiments targeting FLNAD21-D23 to dendritic spines by using a spine-targeting domain (such as of SG2NA (Gaillard et al., 2006)) to inhibit PHD2 locally in the spines could be designed to confirm the model that PHD2 activity, locally at the spines, mediates spine maturation.

PHD2 TARGETS FLNA FOR PROTEASOMAL DEGRADATION

PHDs orchestrate the levels of target proteins via hydroxylation of prolines, though hydroxylation-independent activities have also been reported (Wong et al., 2013). Using a combination of biochemical, imaging and site-directed mutagenesis methods, we show that PHD2 interacts with domains D21-D23 of FLNA, and hydroxylates P2309 and P2316 (conserved in zebrafish, mouse, rat, human), favoring its ubiquitination and proteasomal degradation. This FLNA/PHD2/VHL machinery is present in PSDs of dendritic spines. Inactivation of PHD2-hydroxylation activity or mutation of P2309 and P2316 to alanine impaired FLNA hydroxylation. Triple mutation of P2309, P2312 and P2316 reduced the

interaction with VHL. Genetic studies *in vitro* and *in vivo* confirmed the importance of PHD2 and VHL in dendritic spine remodeling. Together, these studies identify FLNA as a target of PHD2, involved in the formation and maturation of dendritic spines.

In immortalized cell lines, hypoxia induces FLNA cleavage (Zheng et al., 2014). However, hypoxia or DMOG did not upregulate such FLNA fragment in MHNs (not shown), perhaps because the effects of hypoxia on FLNA levels are cell type-dependent or differ upon immortalization. In any case, FLNA protein levels in primary MHN were *increased* – not *decreased* – upon exposure to hypoxia or DMOG. Though spine remodeling by PHD2 is HIF-independent, we cannot exclude that other PHD2 targets, apart of FLNA, influence spine remodeling.

PRECISE REGULATION OF FLNA LEVELS

Somewhat counterintuitively, both the modest elevation of FLNA (by mycFLNA$^{D21\text{-}D23\text{-}WT}$) and silencing of *Flna* resulted in similar – though not exactly identical – spine changes. Indeed, silencing of *Flna* increased protrusion length without affecting the protrusion density or the number of spines with head, while MHNs transfected with mycFLNA$^{D21\text{-}D23\text{-}WT}$ had fewer and less mature dendritic spines. This apparent contradiction likely relates to the well known fact that FLNA interacts with several partners and has contextual effects, and that FLNA protein levels require precise regulation. Indeed, both under- and overexpression of *FLNA* impair neuronal migration, though via distinct molecular mechanisms (Sarkisian et al., 2006; Zhang et al., 2013; Zhang et al., 2012). Even more, both loss and gain of *FLNA/cheerio* in humans and flies cause resembling neurological defects, though distinct symptoms have also been reported (Bolduc et al., 2010; Zhou et al., 2010). All this suggests that FLNA protein levels must be tightly regulated in neurons. Our findings that FLNA is post-translationally regulated by PHD2-mediated hydroxylation and VHL-mediated ubiquitination unravel a molecular mechanism for the precise regulation of FLNA abundance, required for proper formation and maintenance of synapses.

PHYSIOLOGICAL RELEVANCE: A HYPOTHESIS?

Our findings that hypoxia rapidly induces reversible spine regression may help to better understand how neurons adapt to a hypoxia challenge. Since synaptic transmission is a high energy consuming process and neurons rely on oxygen to produce ATP, one possible mechanism whereby neurons can avoid an energy crisis, is by decreasing synaptic transmission through spine regression. Importantly, this remodeling is not irreversible (which would otherwise impair brain performance permanently), but PHD2/FLNA may provide a molecular mechanism for reversible spine maturation and re-establishment of synapses upon return to sufficient oxygen conditions. While our study was not designed to provide direct proof for such a protective mechanism, previous reports support this hypothesis. First, when ATP production is compromised, dendritic arborization is impaired (Oruganty-Das et al., 2012). Second, both an increase in spine length and a rapid reversible spine retraction protect against excitotoxic damage in hypoxia (Araya et al., 2006; Meller et al., 2008). Third, in hypoperfused peri-infarct regions, neurons lower the number of mature spines and increase the length of protrusions to protect against excitotoxic overstimulation and to rewire new functional circuits (Brown et al., 2010).

EXPERIMENTAL PROCEDURES

Detailed methods are described in the Supplemental Experimental Procedures.

ANIMALS

Animal housing and procedures were approved by the Animal Ethics Committee of KU Leuven. We used Swiss, *Phd2*$^{lox/lox}$, PHD2^{KO}, *Nestin*Cre, *Vhl*$^{lox/lox}$ and *Hif-1α*$^{lox/lox}$ mice and Wistar rats. *In utero* electroporations were performed at E15.5. Pups were exposed to 8% O_2 for 4 hrs.

CELL CULTURE

Hippocampal neurons were isolated and cultured as described (Segura et al., 2007). Dendritic spines were analyzed at 14 DIV and synaptic densities at 21 DIV. HEK293T and rat PC12 cells were cultured as described. Hypoxic incubations were at 0.5-1% (neurons) or 0.2% O_2 (HEK293T). Transfections were done by Lipofectamine2000 (neurons), calcium phosphate (HEK293T) or Nucleofection (PC12); transductions were done as described in Supplement.

RNA AND PROTEIN ANALYSIS

IMMUNOBLOTTING, IMMUNOPRECIPITATIONS AND PULL-DOWNS were done as described. RNA EXPRESSION analysis was done by *in situ* hybridization, RT-PCR or RNA-seq. IMMUNOSTAINING was performed on 4% PFA fixed hippocampal neurons or thick free-floating brain cryo- or vibratome sections.

MASS SPECTROMETRY

HEK293T cells transfected with mycFLNA$^{D21\text{-}D23\text{-}WT}$ with or without PHD2^{WT}YFP were incubated with vehicle or 10 μM MG132 for 2 hrs before lysis. Cell lysates were immunoprecipitated with anti-myc antibodies and fractionated by SDS-PAGE. The section containing mycFLNA$^{D21\text{-}D23\text{-}WT}$ was trypsinized in gel and digested peptides were analyzed by nano LC-MS/MS.

IMAGING, TIME-LAPSE AND QUANTIFICATIONS

Bright field, fluorescent, (time-lapse) confocal imaging, super-resolution imaging (SR-SIM), transmission electron microscopy (TEM) and time-domain fluorescence lifetime imaging microscopy (FLIM) were performed as described in Supplement. Morphometry (NIH ImageJ) was done blinded for the experimental conditions.

CELLULAR AND NETWORK ELECTROPHYSIOLOGY

Patch-clamp recordings in MHNs were performed as described (Reinartz et al., 2014). Extracellular recordings of the spontaneous network-level electrical activity, arising among neurons growing over MEAs were performed as reported (Gambazzi et al., 2010).

STATISTICS

Experiments were performed at least three times. Data are expressed as mean ± SEM. Statistical differences were calculated by two-tailed unpaired *t*-test for two data sets or ANOVA followed by Bonferroni *posthoc* test for multiple data sets using Prism (GraphPad Inc). Statistical differences on data from MEAs were calculated by the Wilcoxon rank sum test. $p < 0.05$ was considered statistically significant.

AUTHORS CONTRIBUTIONS

PC conceptualized; IS, CL, EK, AM, RP, TC, CT, CB and BG, performed experiments and analyzed data. IS, CL, EK, AM, RP, GE, TC, CT, MM, BG, MG, CRA, MD and PC designed experiments. DD and MH provided technical infrastructure, reagents and expertise. IS, CL, MD and PC wrote the manuscript. All authors edited the paper.

ACKNOWLEDGEMENTS

We thank MS. Ramer, L. Moons, R. Klein and P. Maxwell; R. Klein (MPI, Germany) for the *Nestin*Cre mice, J. Blenis (Harvard) for pcDNA3-myc-hFLNA-WT, J. Goedhart (Amsterdam) for Turquoise2 plasmids, J. Livet (Paris) for the Brainbow1.0 plasmid, W. Kaelin (Harvard) for the HA-VHL plasmid and J. de Wit (KU Leuven) for the vGlut1 antibody. We acknowledge L. Notebaert, M. Wijnants, D. van Dick, technical staff and VRC core facilities. IS was supported by the Marie Curie FP7 program. IS and CL are postdoctoral fellows of the Research Foundation–Flanders (FWO). CT was supported by an ERC Starting Grant (281961–ASTROFUNC) to MH. This work was supported by the Belgian Science Policy (grant IAP-P6/20 to MD and IAP-P7/20 to MD and MG), by EC-FP7 grants (264872–NAMASEN; 306502–BRAINLEAP and 286403–NEUROACT to MG), grants from the FWO (G.0671.12N to PC, 1.5.244.11N to IS, G088812N to MG) and long-term structural Methusalem funding by the Flemish Government and the Foundation Leducq Transatlantic Network (ARTEMIS) to PC.

CONFLICT-OF-INTEREST DISCLOSURE: The authors declare no conflict of interest.

REFERENCES

Araya, R., Jiang, J., Eisenthal, K.B., and Yuste, R. (2006). The spine neck filters membrane potentials. Proc Natl Acad Sci U S A *103*, 17961-17966.

Bolduc, F.V., Bell, K., Rosenfelt, C., Cox, H., and Tully, T. (2010). Fragile x mental retardation 1 and filamin a interact genetically in Drosophila long-term memory. Front Neural Circuits *3*, 22.

Brown, C.E., Boyd, J.D., and Murphy, T.H. (2010). Longitudinal in vivo imaging reveals balanced and branch-specific remodeling of mature cortical pyramidal dendritic arbors after stroke. J Cereb Blood Flow Metab *30*, 783-791.

Cho, K.O., Hunt, C.A., and Kennedy, M.B. (1992). The rat brain postsynaptic density fraction contains a homolog of the Drosophila discs-large tumor suppressor protein. Neuron *9*, 929-942.

Corcoran, A., Kunze, R., Harney, S.C., Breier, G., Marti, H.H., and O'Connor, J.J. (2013). A role for prolyl hydroxylase domain proteins in hippocampal synaptic plasticity. Hippocampus *23*, 861-872.

Epstein, A.C., Gleadle, J.M., McNeill, L.A., Hewitson, K.S., O'Rourke, J., Mole, D.R., Mukherji, M., Metzen, E., Wilson, M.I., Dhanda, A.*, et al.* (2001). C. elegans EGL-9 and mammalian homologs define a family of dioxygenases that regulate HIF by prolyl hydroxylation. Cell *107*, 43-54.

Erecinska, M., and Silver, I.A. (2001). Tissue oxygen tension and brain sensitivity to hypoxia. Respir Physiol *128*, 263-276.

Ethell, I.M., and Pasquale, E.B. (2005). Molecular mechanisms of dendritic spine development and remodeling. Prog Neurobiol *75*, 161-205.

Gaillard S, Bailly Y, Benoist M, Rakitina T, Kessler JP, Fronzaroli-Molinières L, Dargent B, Castets F. Targeting of proteins of the striatin family to dendritic spines: role of the coiled-coil domain. Traffic *7*, 74-84

Gambazzi, L., Gokce, O., Seredenina, T., Katsyuba, E., Runne, H., Markram, H., Giugliano, M., and Luthi-Carter, R. (2010). Diminished activity-dependent brain-derived neurotrophic factor expression underlies cortical neuron microcircuit hypoconnectivity resulting from exposure to mutant huntingtin fragments. J Pharmacol Exp Ther *335*, 13-22.

Hotulainen, P., and Hoogenraad, C.C. (2010). Actin in dendritic spines: connecting dynamics to function. J Cell Biol *189*, 619-629.

Ivan, M., Kondo, K., Yang, H., Kim, W., Valiando, J., Ohh, M., Salic, A., Asara, J.M., Lane, W.S., and Kaelin, W.G., Jr. (2001). HIFalpha targeted for VHL-mediated destruction by proline hydroxylation: implications for O2 sensing. Science *292*, 464-468.

Jaakkola, P., Mole, D.R., Tian, Y.M., Wilson, M.I., Gielbert, J., Gaskell, S.J., von Kriegsheim, A., Hebestreit, H.F., Mukherji, M., Schofield, C.J.*, et al.* (2001). Targeting of HIF-alpha to the von Hippel-Lindau ubiquitylation complex by O2-regulated prolyl hydroxylation. Science *292*, 468-472.

Mazzone, M., Dettori, D., Leite de Oliveira, R., Loges, S., Schmidt, T., Jonckx, B., Tian, Y.M., Lanahan, A.A., Pollard, P., Ruiz de Almodovar, C.*, et al.* (2009). Heterozygous deficiency of PHD2 restores tumor oxygenation and inhibits metastasis via endothelial normalization. Cell *136*, 839-851.

Meller, R., Thompson, S.J., Lusardi, T.A., Ordonez, A.N., Ashley, M.D., Jessick, V., Wang, W., Torrey, D.J., Henshall, D.C., Gafken, P.R.*, et al.* (2008). Ubiquitin proteasome-

mediated synaptic reorganization: a novel mechanism underlying rapid ischemic tolerance. J Neurosci *28*, 50-59.

Nakamura, F., Stossel, T.P., and Hartwig, J.H. (2011). The filamins: organizers of cell structure and function. Cell Adh Migr *5*, 160-169.

Nestor, M.W., Cai, X., Stone, M.R., Bloch, R.J., and Thompson, S.M. (2011). The actin binding domain of betaI-spectrin regulates the morphological and functional dynamics of dendritic spines. PLoS One *6*, e16197.

Noam, Y., Phan, L., McClelland, S., Manders, E.M., Ehrengruber, M.U., Wadman, W.J., Baram, T.Z., and Chen, Y. (2012). Distinct regional and subcellular localization of the actin-binding protein filamin A in the mature rat brain. J Comp Neurol *520*, 3013-3034.

Nwabuisi-Heath, E., LaDu, M.J., and Yu, C. (2012). Simultaneous analysis of dendritic spine density, morphology and excitatory glutamate receptors during neuron maturation in vitro by quantitative immunocytochemistry. J Neurosci Methods *207*, 137-147.

Oruganty-Das, A., Ng, T., Udagawa, T., Goh, E.L., and Richter, J.D. (2012). Translational control of mitochondrial energy production mediates neuron morphogenesis. Cell Metab *16*, 789-800.

Pacary, E., Haas, M.A., Wildner, H., Azzarelli, R., Bell, D.M., Abrous, D.N., and Guillemot, F. (2012). Visualization and genetic manipulation of dendrites and spines in the mouse cerebral cortex and hippocampus using in utero electroporation. J Vis Exp *Jul 26*, pii: 4163.

Reinartz, S., Biro, I., Gal, A., Giugliano, M., and Marom, S. (2014). Synaptic dynamics contribute to long-term single neuron response fluctuations. Front Neural Circuits *8*, 71.

Sarkisian, M.R., Bartley, C.M., Chi, H., Nakamura, F., Hashimoto-Torii, K., Torii, M., Flavell, R.A., and Rakic, P. (2006). MEKK4 signaling regulates filamin expression and neuronal migration. Neuron *52*, 789-801.

Segura, I., Essmann, C.L., Weinges, S., and Acker-Palmer, A. (2007). Grb4 and GIT1 transduce ephrinB reverse signals modulating spine morphogenesis and synapse formation. Nat Neurosci *10*, 301-310.

Song, D., Li, L.S., Heaton-Johnson, K.J., Arsenault, P.R., Master, S.R., and Lee, F.S. (2013). Prolyl hydroxylase domain protein 2 (PHD2) binds a Pro-Xaa-Leu-Glu motif, linking it to the heat shock protein 90 pathway. J Biol Chem *288*, 9662-9674.

Stossel, T.P., Condeelis, J., Cooley, L., Hartwig, J.H., Noegel, A., Schleicher, M., and Shapiro, S.S. (2001). Filamins as integrators of cell mechanics and signalling. Nat Rev Mol Cell Biol *2*, 138-145.

Tashiro, A., and Yuste, R. (2004). Regulation of dendritic spine motility and stability by Rac1 and Rho kinase: evidence for two forms of spine motility. Mol Cell Neurosci *26*, 429-440.

Tsuchiya, H., Iseda, T., and Hino, O. (1996). Identification of a novel protein (VBP-1) binding to the von Hippel-Lindau (VHL) tumor suppressor gene product. Cancer Res *56*, 2881-2885.

van der Flier, A., and Sonnenberg, A. (2001). Structural and functional aspects of filamins. Biochim Biophys Acta *1538*, 99-117.

Vogel, S., Wottawa, M., Farhat, K., Zieseniss, A., Schnelle, M., Le-Huu, S., von Ahlen, M., Malz, C., Camenisch, G., and Katschinski, D.M. (2010). Prolyl hydroxylase domain (PHD) 2 affects cell migration and F-actin formation via RhoA/rho-associated kinase-dependent cofilin phosphorylation. J Biol Chem *285*, 33756-33763.

Wong, B.W., Kuchnio, A., Bruning, U., and Carmeliet, P. (2013). Emerging novel functions of the oxygen-sensing prolyl hydroxylase domain enzymes. Trends Biochem Sci *38*, 3-11.

Zhang, J., Neal, J., Lian, G., Hu, J., Lu, J., and Sheen, V. (2013). Filamin A regulates neuronal migration through brefeldin A-inhibited guanine exchange factor 2-dependent Arf1 activation. J Neurosci *33*, 15735-15746.

Zhang, J., Neal, J., Lian, G., Shi, B., Ferland, R.J., and Sheen, V. (2012). Brefeldin A-inhibited guanine exchange factor 2 regulates filamin A phosphorylation and neuronal migration. J Neurosci *32*, 12619-12629.

Zhang, L., Bartley, C.M., Gong, X., Hsieh, L.S., Lin, T.V., Feliciano, D.M., and Bordey, A. (2014). MEK-ERK1/2-dependent FLNA overexpression promotes abnormal dendritic patterning in tuberous sclerosis independent of mTOR. Neuron *84*, 78-91.

Zheng, L., Michelson, Y., Freger, V., Avraham, Z., Venken, K.J., Bellen, H.J., Justice, M.J., and Wides, R. (2011). Drosophila Ten-m and filamin affect motor neuron growth cone guidance. PLoS One *6*, e22956.

Zheng, X., Zhou, A.X., Rouhi, P., Uramoto, H., Boren, J., Cao, Y., Pereira, T., Akyurek, L.M., and Poellinger, L. (2014). Hypoxia-induced and calpain-dependent cleavage of filamin A regulates the hypoxic response. Proc Natl Acad Sci U S A *111*, 2560-2565.

Zhou, A.X., Hartwig, J.H., and Akyurek, L.M. (2010). Filamins in cell signaling, transcription and organ development. Trends Cell Biol *20*, 113-123.

FIGURE LEGENDS

FIGURE 1: EFFECT OF HYPOXIA ON DENDRITIC SPINES

In all panels, N: normoxia, H: hypoxia (1% O_2 (A-E) or 0.5% O_2 (F-H)). **A-B',** YFP-transfected MHNs were incubated for 16 hrs in normoxia (A) or hypoxia (B) and analyzed for protrusion density (C), protrusion length (D) and percentage of spines with head (E) (n = 3 experiments, 30 neurons, > 800 protrusions). A',B' Higher magnifications of the box in A or B. **F,** Snap-shot images at the start (0) and after 15, 30, 45 or 60 min of time-lapse recording of 14 DIV tdT-labeled MHNs, in control (upper) or hypoxia (lower). Solid arrowheads: spines with persistent increase or decrease in length; open arrowheads: spines that do not change their length. Each color denotes a distinct spine. Red asterisk indicates a sprouting dendrite. **G,H,** Length of protrusions at 0 and 1 hr recording in normoxia or hypoxia (G; n ≥ 40) and distribution of spines according to length variation (H). Stable: Δ-length ≤ 0.2 µm. Mean ± SEM. ***p < 0.001. Scale bar: 10 µm (A-B'), 5 µm (F). See Fig. S1 and S2.

FIGURE 2: SYNAPTIC ACTIVITY AND DENSITY OF MHNS IN HYPOXIA AND DMOG.

In all panels, N: normoxia, H: hypoxia (1% O_2), H/N: hypoxia o/n followed by 24 hrs normoxia, D: DMOG (250 µM (A,B,G,G') or 1 mM (C,D)), WO: washout. **A,** Spontaneous action potential (AP) firing recorded from single cells by patch-clamp. **B,** Representative APs recorded by patch-clamp. **C,D**, Frequency of spontaneous AP firing (C) and network-wide AP synchronization (D) (n = 4 MEAs/condition) in MHN in the indicated conditions. **E-H,** vGlut (green) and PSD-95 (red) immunostaining (E'-G') of tdT-transfected MHN (E-G) that were subjected at 20 DIV for 16 hrs to the indicated conditions; the contour of the dendrite in E-G is indicated in E'-G'. Quantification of dendritic density of $vGlut^+/PSD\text{-}95^+$ co-clusters (H; n ≥ 20 neurons) (by counting the yellow clusters and the red clusters in immediate apposition with the dendrite/spine). Mean ± SEM. *p < 0.05 *versus* normoxia (A) or *versus* their respective 13 DIV value (C,D); ***p < 0.001. Scale bar: 10 µm. See Fig. S3.

FIGURE 3: PHD2 EXPRESSION AND SILENCING IN DENDRITIC SPINES

A, Representative IB of non-PSD fraction (NS), synaptic membranes (S) and postsynaptic density (PSD) enriched fractions for the indicated proteins. **B,** Staining of MHNs for PHD2 (green) and synaptophysin (red). Lower panels are higher magnifications (lower left: $PHD2^+$ signal; lower right: merged signal). Arrowheads: $PHD2^+$ postsynaptic clusters. Dotted lines: neighbouring cells (high-density cultures were used to maintain neurons in culture for prolonged periods); green/red dots outside the soma and dendrite are stainings of neighbouring cells. **C-I,** 13 DIV MHN co-transfected with YFP plus control shRNA (scr) (C,E) or shPhd2 (D,F) were incubated for 16 hrs in normoxia (C,D) or hypoxia (E,F) and analyzed for protrusion density (G), protrusion length (H) and % of spines with head (I) (n = 3 experiments, 21-30 neurons, 300-1400 protrusions). **J-L,** vGlut (green) and PSD-95 (red) immunostaining (J',K') of MHNs co-transfected at 14 DIV with scr (J,J') or shPhd2 (K,K') together with tdT (J-L'); the contour of the dendrite in J,K is indicated in J',K'. Quantification of dendritic density of $vGlut^+$/$PSD\text{-}95^+$ co-clusters (L; n ≥ 20 neurons). **M-Q,** YFP-transfected 14 DIV MHNs isolated from control (M) or $PHD2^{NKO}$ (N) littermates, and analyzed for protrusion density (O), protrusion length (P) and number of spines with head (Q; n = 6 animals, >30 dendrites, >1,000 protrusions). **R,** Frequency of spontaneous network-wide AP synchronization (n = 4 MEAs/condition) of 14DIV MHNs isolated from ctrl or $PHD2^{NKO}$ littermates. **S,** Representative dendritic protrusions of 14 DIV MHN isolated from ctrl or $PHD2^{NKO}$ littermates upon transfection at 7 DIV with YFP (upper panels), $PHD2^{WT}$YFP (lower left) or $PHD2^{MUT}$YFP (lower right). **T,** Analysis of dendritic protrusion density in CA1 region of 2-wks old WT mice upon *in utero* electroporation at E15.5 with control shRNA (scr) or shPhd2 (n = 4-6 animals). Mean ± SEM (G-I,L,O-R) or single data plus mean ± SEM (T). *p < 0.05, **p < 0.01, ***p < 0.001. Scale bars: 10 µm (B), 5 µm (C-F,J-K',M,N,S). See Fig. S4, S5 and S6.

FIGURE 4: FILAMIN A EXPRESSION IN DENDRITIC SPINES

A, SIM micrograph of YFP^+ (green) RHN, immunostained for endogenous FLNA (red; gray in right panels). Arrowheads: $FLNA^+$ puncta in filopodium (upper panels); green dashed

line: contour of a dendritic spine head (lower panels). **B,** 14 DIV MHN co-transfected with tdT (red) and FLNA^{FL}TQ2 (green) in normoxia or hypoxia. **C,** Representative immunoblot (IB) for FLNA, VHL and drebrin of mouse brain homogenate (H), non-synaptic fraction (NS), synaptic membranes (S) and PSD enriched fractions from WT mice exposed to normoxia or hypoxia (8% O_2) for 4 hrs. **D,** Representative IB for FLNA and tubulin in 14 DIV MHNs subjected to normoxia or hypoxia for the indicated time points. **E,** Representative IB for FLNA and tubulin in 14 DIV untreated MHN or treated with DMOG for 2 hrs. **F,** Representative IB for FLNA and tubulin in untreated MHNs (-) or treated with DMOG (D), MG132 (MG), actinomycin D (Ac) or cycloheximide (Cy), in normoxia or hypoxia. **G,** Representative IB for FLNA and tubulin in MHN treated for 2 hrs with increasing concentrations of MG132. **H,** IB for FLNA, PHD2, myc and tubulin in MHNs transduced with scrambled control shRNA (scr), shPhd2 or overexpressing mycFLNA$^{D21-D23-WT}$. **I,** Representative IB for the indicated proteins of mouse brain homogenate (H), non-synaptic fraction (NS), synaptic membranes (S) and PSD enriched fractions obtained from control (ctrl) or PHD2^{NKO} littermates. Synaptop.: synaptophysin. Densitometry of IBs as shown in panels C-I are shown in Fig. S7. Scale bar: 1 µm (A), 10 µm (B). See Fig. S7.

FIGURE 5: ANALYSIS OF FILAMIN A AS PHD2 TARGET

A, Representative immunoblot (IB) for YFP and myc after immunoprecipitation (IP) of mycFLNA^{FL} from HEK293T cells co-expressing mycFLNA^{FL} and PHD2^{WT}YFP or PHD2^{MUT}YFP. Total lysates are shown below. **B,** Representative IB for FLNA and PHD2 after IP of PHD2 in mouse brain homogenate (H), non-synaptic fraction (NS), synaptic membranes (S) and PSD fractions. Total lysates are shown below. **C,** Top: Diagrams of the domains of full-length (FL) and deletion constructs of FLNA. ABD: actin binding domain; 1-24: IgG-repeats; H1,H2: hinges. Bottom: Representative IB for myc and YFP after IP of myc-tagged FLNA deletion mutants co-expressed with PHD2^{MUT}YFP in HEK293T cells. Arrows: myc-tagged proteins and PHD2^{MUT}YFP; asterisks: aspecific bands. **D,** Representative fluorescence lifetime images (FLIM) and life time measurements of FLNA^{CT}TQ2 when transfected alone or in combination with YFP, PHD2^{WT}YFP or

PHD2^{MUT}YFP in HEK293T cells (mean ± SEM; n ≥ 50 cells). **E,** Representative IB for hydroxyprolines (OH-Pro) or myc after IP of mycFLNA^{FL} from HEK293T cells transfected with mycFLNA^{FL} and treated for 2 hrs with MG132 (MG) or lactacystin (L). Total lysates are shown below. **F,** Representative IB and densitometric quantification for FLNA and OH-Pro after IP with control IgG (left) or specific antibodies for FLNA (right) of brain homogenates from P10 rats housed in control (ctrl) or hypoxia (H) chambers. **G,** MS/MS fragmentation spectra of unmodified (panel a; from control HEK293T cells) and hydroxylated (panel b; from PHD2^{WT}YFP-transfected HEK293T cells, treated with MG132 for 2 hrs) P2316 in FNEEHIPDSPFVVPVASPSGDAR of FLNA, focusing on the fragment ion (y10), showing a mass shift of 16 Da upon hydroxylation. Complete spectra: Fig. S8G. **H,** Representative IB for the indicated proteins after IP of myc in HEK293T cells co-transfected with PHD2^{WT}YFP together with mycFLNA$^{D21\text{-}D23\text{-}WT}$, mycFLNA$^{D21\text{-}D23\text{-}P2309A}$ or mycFLNA$^{D21\text{-}D23\text{-}P2316A}$ and subjected to control (ctrl; left) or DMOG (right) treatment. Total lysates are shown below. See Fig. S8.

FIGURE 6: ANALYSIS OF FILAMIN A INTERACTION WITH VHL

A, Representative immunoblot (IB) for myc and HA after immunoprecipitation (IP) of myc from HEK293T cells transfected with mycFLNA^{FL} and HA-VHL. Total lysates are shown below. **B,** Representative IB for myc and HA after IP of myc from HEK293T cells transfected with mycFLNA^{CT}, mycFLNA$^{D21\text{-}D23\text{-}WT}$ or mycFLNA$^{H2\text{-}D24}$ together with HA-VHL (left). Total lysates are shown (right). Arrows: myc-tagged proteins; asterisks: IgGs used for the IP. **C,** Representative IB for myc and HA after IP of myc from HEK293T cells transfected with HA-VHL alone or co-transfected with mycFLNA$^{D21\text{-}D23\text{-}WT}$, mycFLNA$^{D21\text{-}D23\text{-}P2309A}$, mycFLNA$^{D21\text{-}D23\text{-}P2316A}$ or mycFLNA$^{D21\text{-}D23\text{-}3P\rightarrow A}$ mutants. Total lysates are shown below. **D,** Representative IB for FLNA and tubulin in MHNs transduced with a control shRNA (scr) or shVhl (left). Densitometric quantification of FLNA protein levels (right; mean ± SEM, n = 3, *p < 0.05). **E,F,** Representative IBs for FLNA, HIF-1α and tubulin (E) or for FLNA, hydroxyprolines (OH-Pro) and tubulin (F) of brain homogenates from E14.5 control (ctrl) or VHL^{NKO} littermates. **G,** Representative IB for FLNA and tubulin after TUBE2

pull-down of brain homogenates obtained from E14.5 control (ctrl) or VHL^{NKO} littermates. Total lysates are shown below. See Fig. S9.

FIGURE 7: EFFECT OF FILAMIN A UPREGULATION ON SPINE MATURATION

A, Representative immunoblot (IB) for FLNA, myc and actin in HEK293T cells under control, hypoxia (0.2% O_2) or after transfection with $mycFLNA^{D21\text{-}D23\text{-}WT}$ (left). Densitometric quantification of FLNA (right). **B,** Representative IB for myc and YFP after immunoprecipitation (IP) of myc in the presence of recombinant GST or $GST\text{-}FLNA^{D21\text{-}D23}$ proteins from homogenates of HEK293T cotransfected with $mycFLNA^{FL}$ and $PHD2^{WT}YFP$. Left (input): Total lysates control in the co-transfected HEK293T. Densitometric quantification of the $PHD2^{WT}YFP/mycFLNA^{FL}$ ratio is shown (n = 3; *p < 0.05). **C-H,** Representative images of tdT^{+} 14 DIV control (ctrl; C), $mycFLNA^{D21\text{-}D23\text{-}WT}$ (D) or $mycFLNA^{D21\text{-}D23\text{-}3P\rightarrow A}$ (E) transfected MHNs. Quantification of protrusion density (F), protrusion length (G) and percentage of spines with head (H) (n = 10 neurons, 324-731 protrusions). **I-L,** Immunostaining of vGlut (green) and PSD-95 (red) (I',J',K') in 21 DIV tdT-transfected MHN (I-K) alone (I,I') or together with $mycFLNA^{D21\text{-}D23\text{-}WT}$ (J,J') or $mycFLNA^{D21\text{-}D23\text{-}3P\rightarrow A}$ (K,K'); the contour of the dendrites in panels I-K is indicated in panels I',J',K'. Quantification of the dendritic density of $vGlut^{+}/PSD\text{-}95^{+}$ co-clusters (L; n ≥ 20 neurons). **M-S,** Representative images of 14 DIV MHN co-transfected with tdT together with scrambled control shRNA (scr) (M), shPhd2 (N), shFlna (O) or both shPhd2 and shFlna (P). Quantification of protrusion density (Q), protrusion length (R) and percentage of spines with head (S) (n ≥ 7 neurons, 7-22 dendrites, 170-832 protrusions). Mean ± SEM. *p < 0.05, ***p < 0.001 (*versus* ctrl or scr); $^{\#}p < 0.05$, $^{\#\#}p < 0.01$, $^{\#\#\#}p < 0.001$ (*versus* shPhd2 or $mycFLNA^{D21\text{-}D23\text{-}WT}$). Scale bar: 5 µm.

Figure 1

Click here to download Figure Figure1-01216.tif

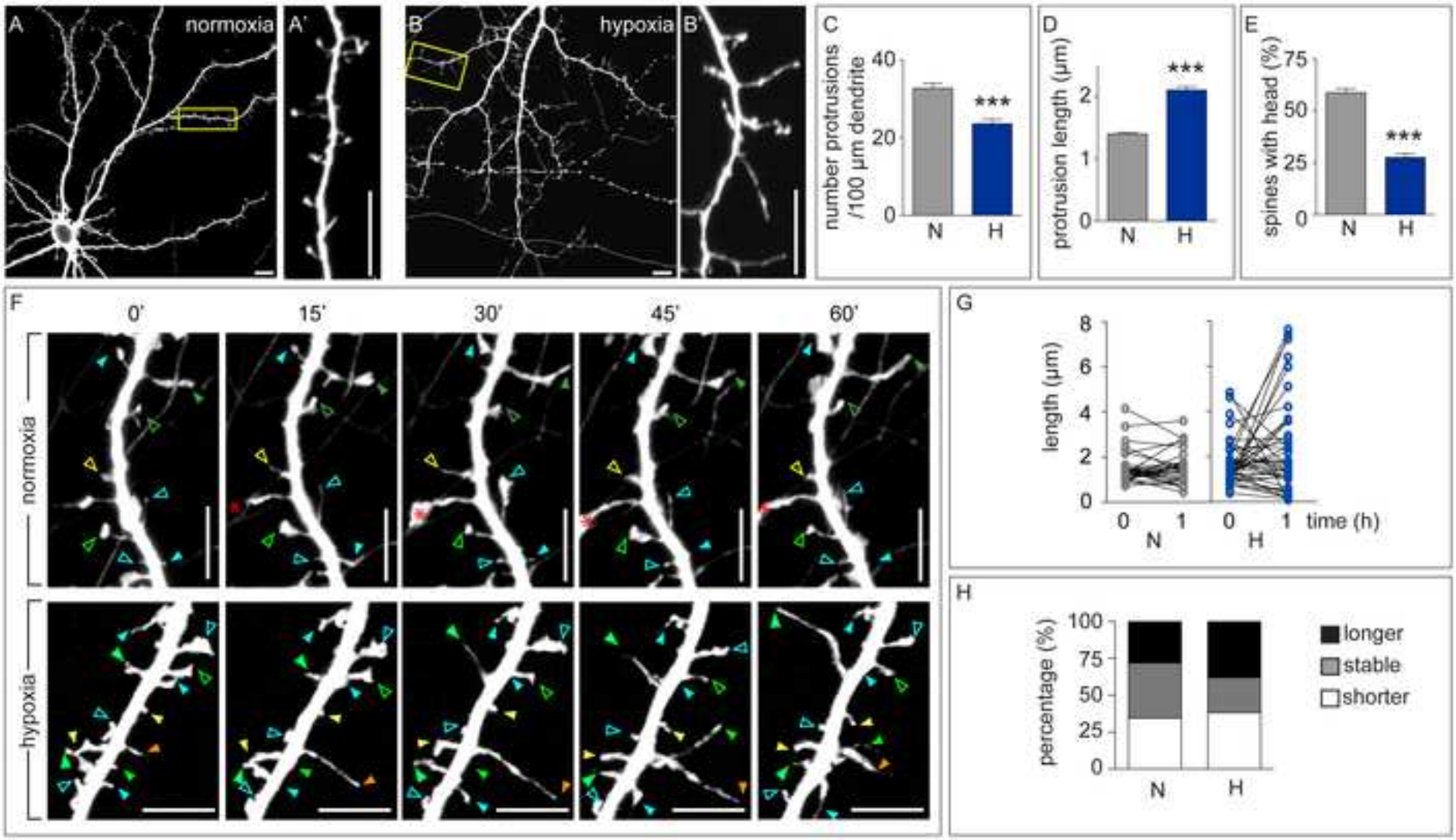

FIGURE 1

Figure 2

Click here to download Figure Figure2-01216.tif

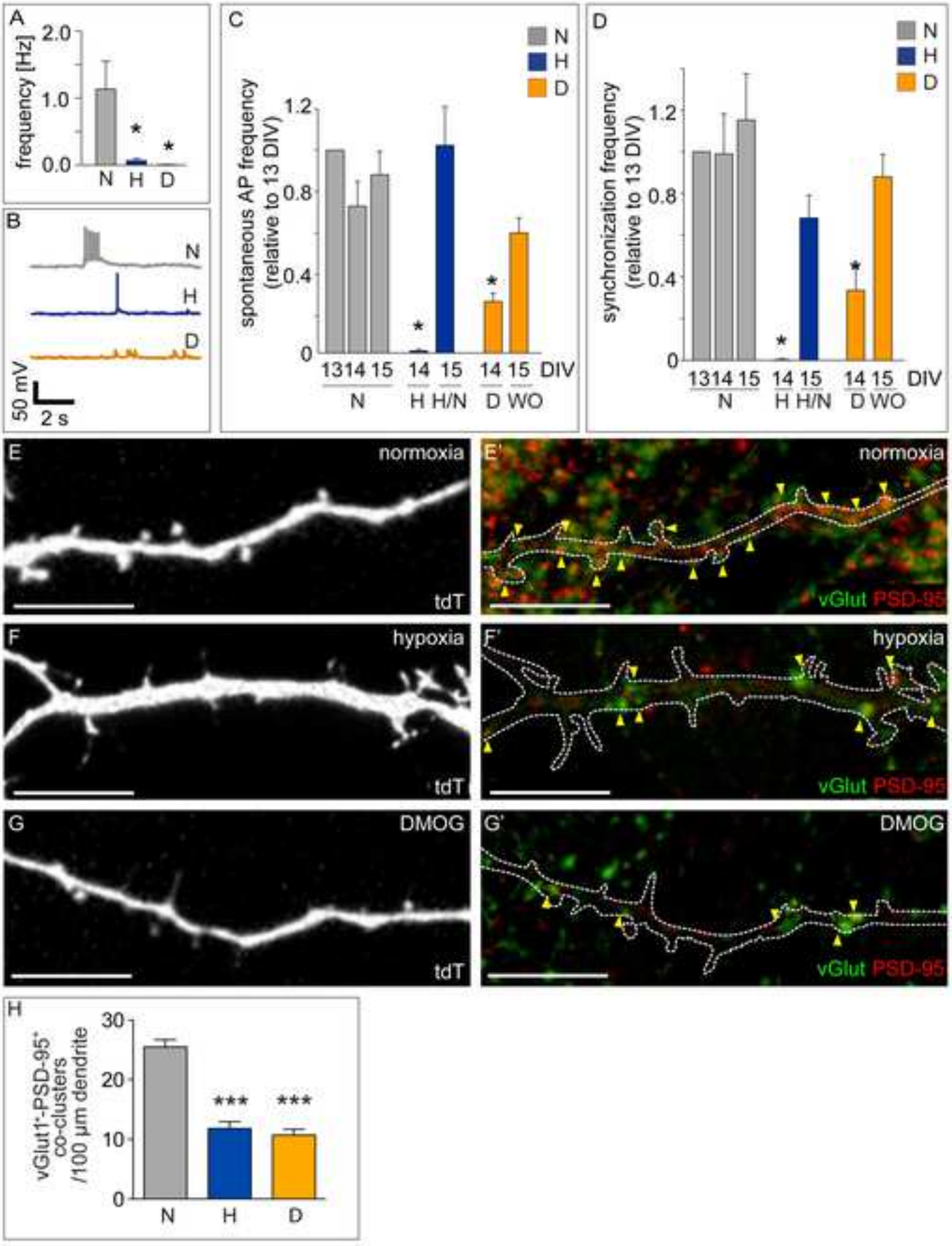

FIGURE 2

Figure 3

Click here to download Figure Figure3_020216.tif

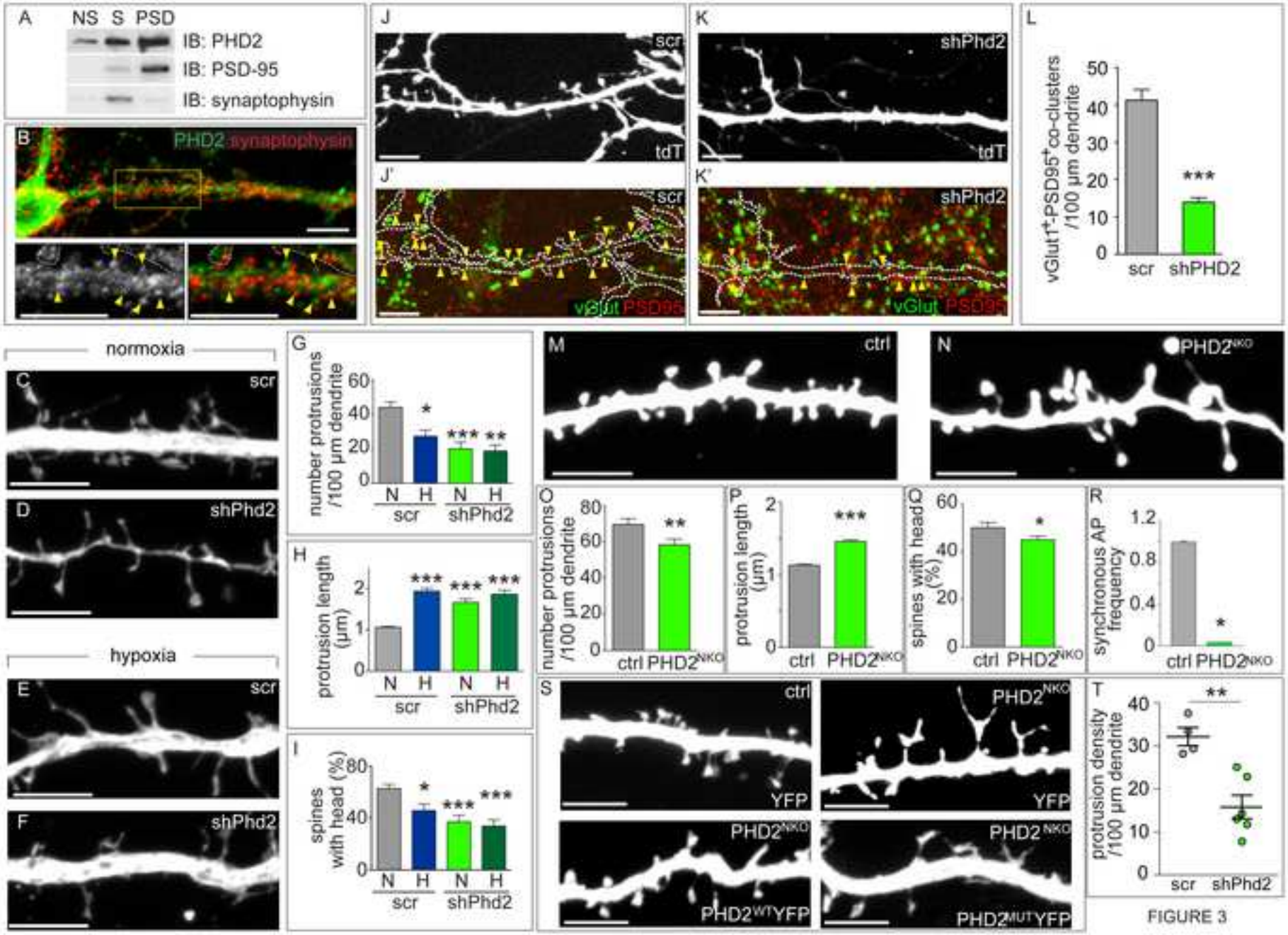

FIGURE 3

Figure 4

Click here to download Figure Figure4_020216.tif

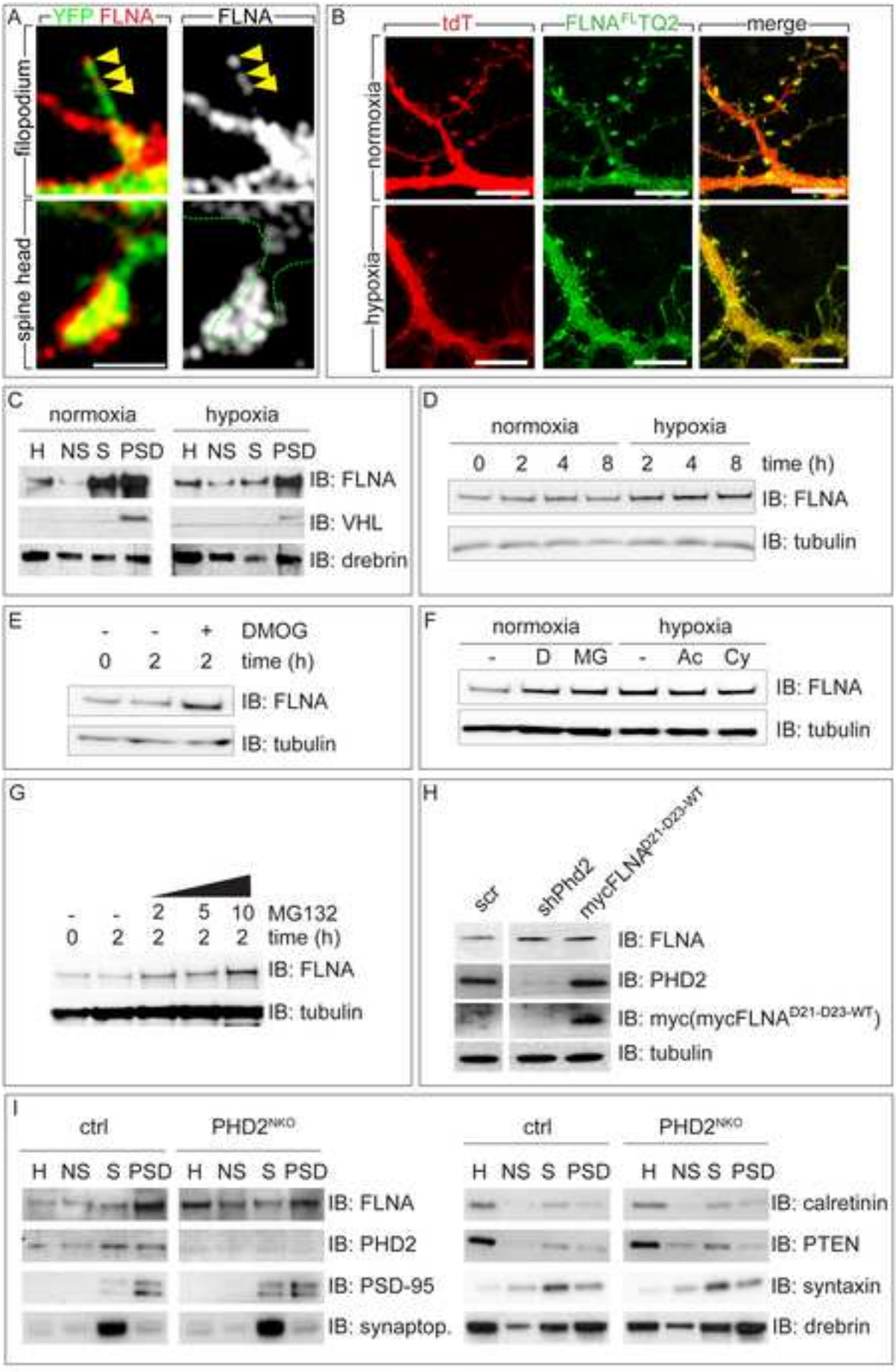

FIGURE 4

Figure 5

Click here to download Figure Figure5_020216.tif

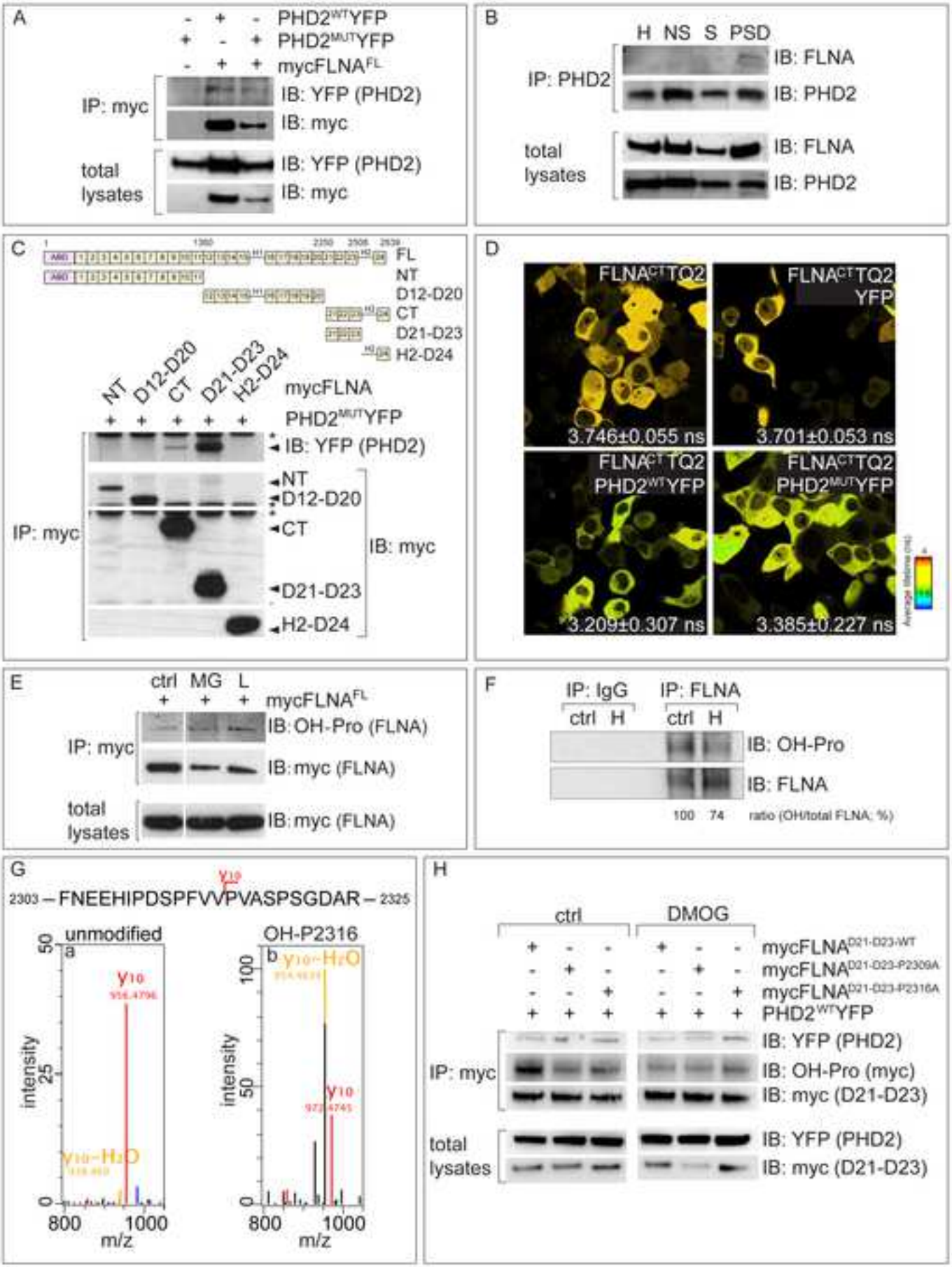

FIGURE 5

Figure 6

Click here to download Figure Figure6_020216.tif

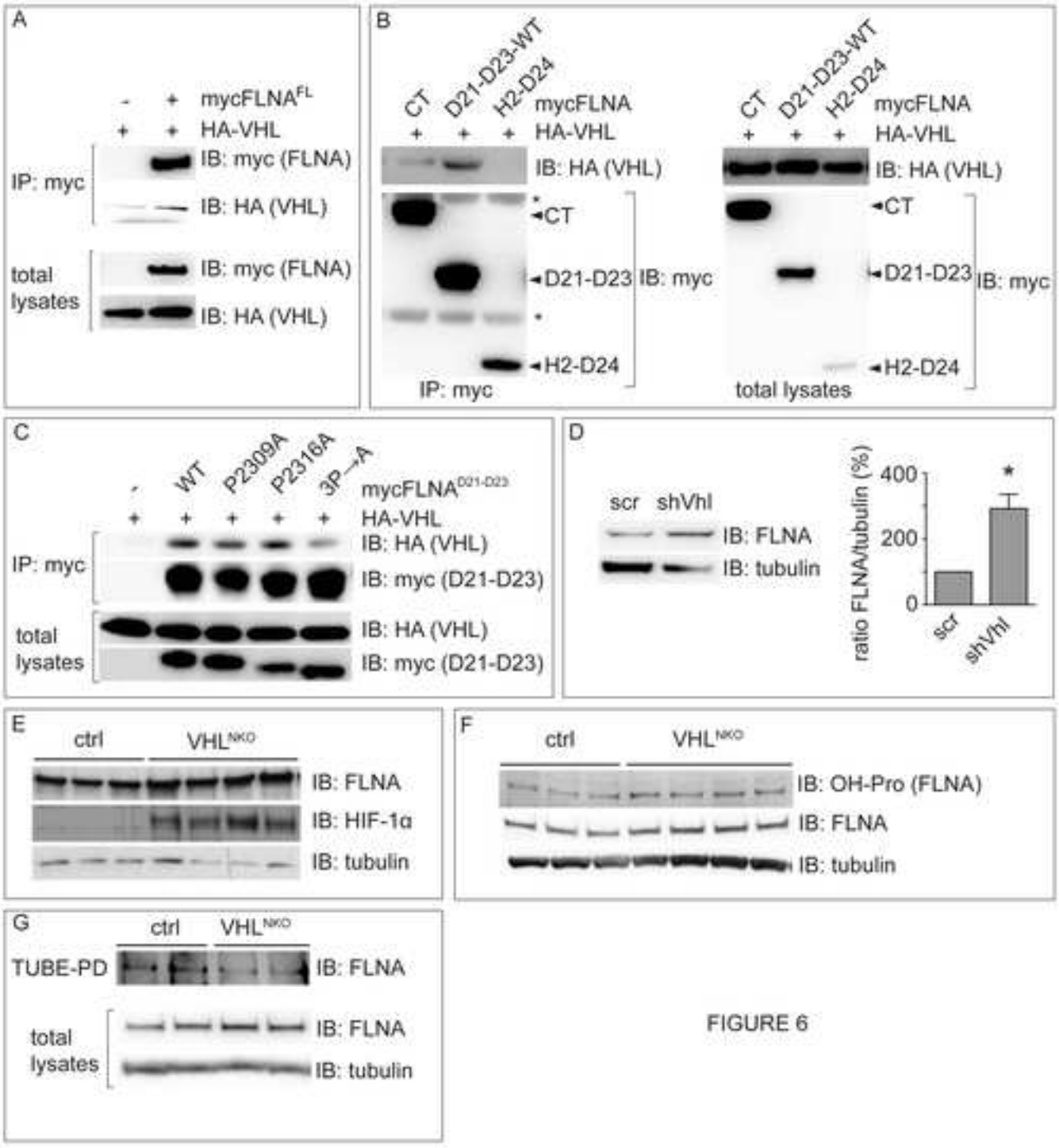

FIGURE 6

Figure 7

Click here to download Figure Figure7_020216.tif

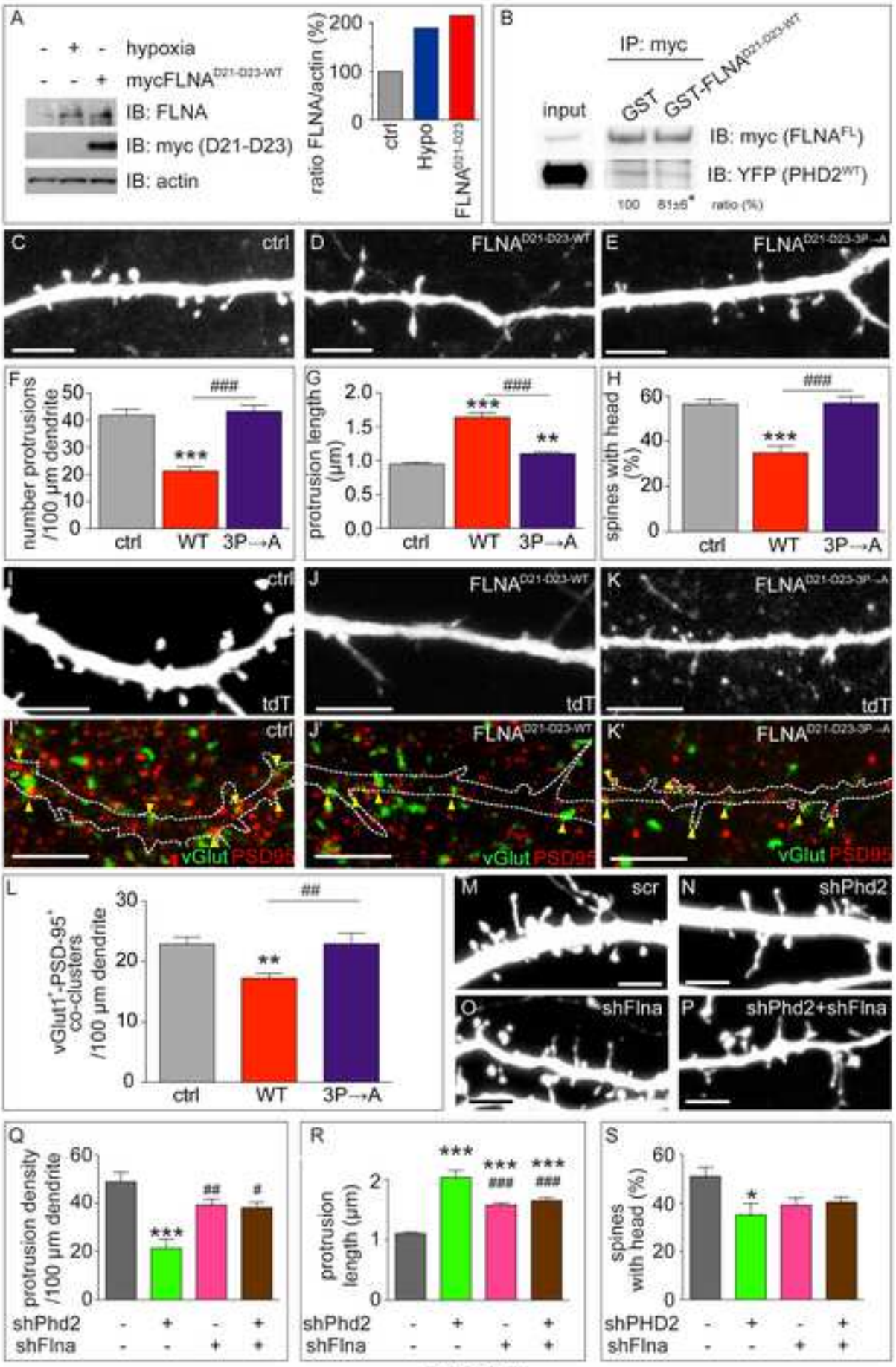

FIGURE 7

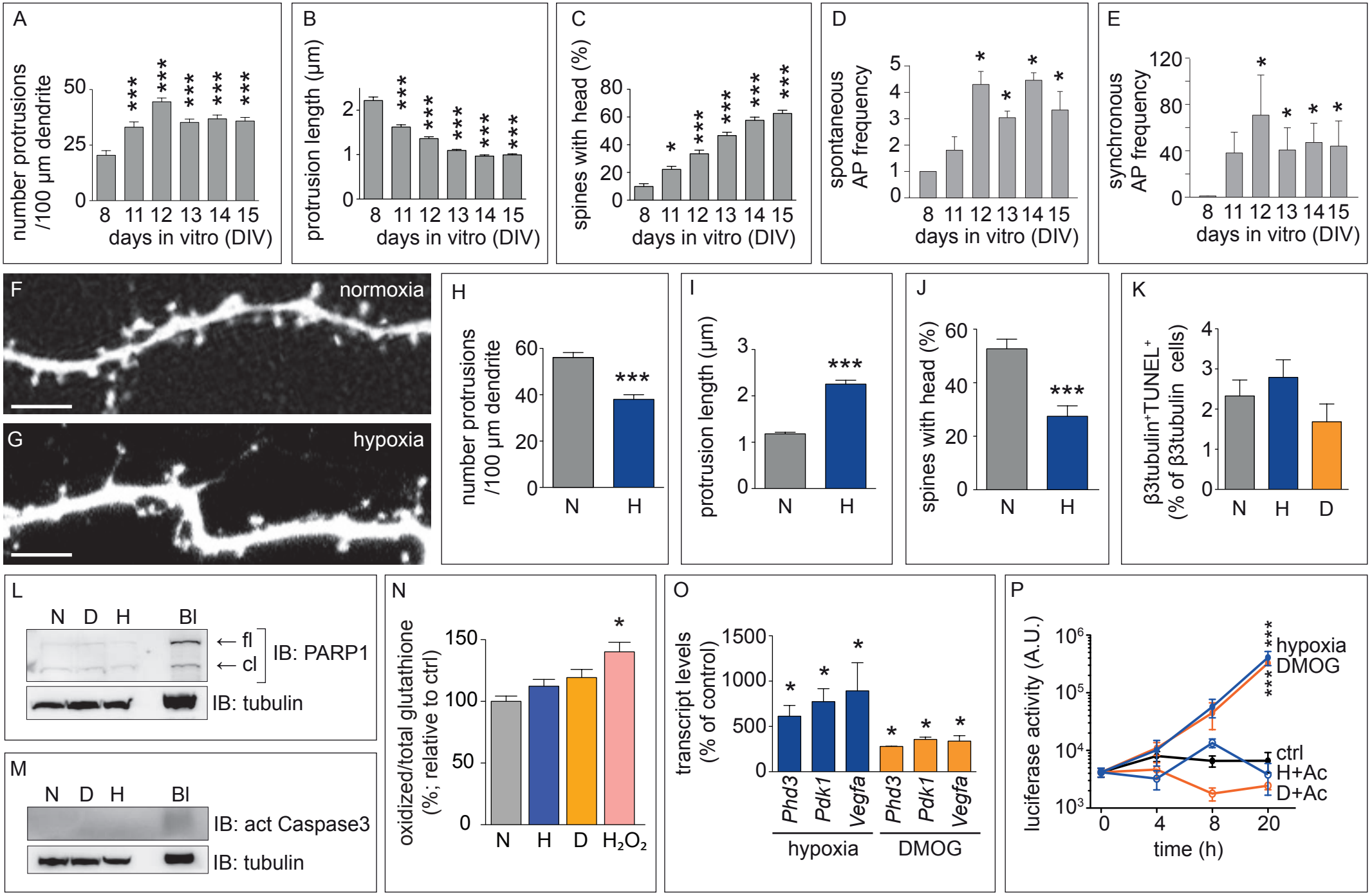
A
number protrusions /100 µm dendrite
50
25
0
8 11 12 13 14 15
days in vitro (DIV)
B
protrusion length (µm)
2
1
0
8 11 12 13 14 15
days in vitro (DIV)
C
spines with head (%)
80
60
40
20
0
8 11 12 13 14 15
days in vitro (DIV)
D
spontaneous AP frequency
5
4
3
2
1
0
8 11 12 13 14 15
days in vitro (DIV)
E
synchronous AP frequency
120
80
40
0
8 11 12 13 14 15
days in vitro (DIV)
F
normoxia
G
hypoxia
H
number protrusions /100 µm dendrite
60
40
20
0
N H
I
protrusion length (µm)
3
2
1
0
N H
J
spines with head (%)
60
40
20
0
N H
K
β3tubulin+TUNEL+ (% of β3tubulin cells)
4
3
2
1
0
N H D
L
N D H BI
← fl
← cl
IB: PARP1
IB: tubulin
M
N D H BI
IB: act Caspase3
IB: tubulin
N
oxidized/total glutathione (%; relative to ctrl)
150
100
50
0
N H D H2O2
O
transcript levels (% of control)
1500
1000
500
0
Phd3 Pdk1 Vegfa Phd3 Pdk1 Vegfa
hypoxia
DMOG
P
luciferase activity (A.U.)
10^6
10^5
10^4
10^3
0 4 8 20
time (h)
hypoxia
DMOG
ctrl
H+Ac
D+Ac

FIGURE S1

FIGURE S1; RELATED TO FIGURE 1

In all panels, N: normoxia, H: hypoxia (1% O_2), D: DMOG (250 μM). **A-C,** Time course analysis of dendritic spines in MHNs *in vitro*. Protrusion density (A), protrusion length (B), and percentage of spines with head (C) was evaluated in tdT labeled dendrites of MHNs at the indicated DIVs (n = 3 experiments, 30 neurons, 30-60 dendrites, 294-762 protrusions). **D,E,** Frequency of spontaneous action potential (AP) firing (D) and network-wide AP synchronization *in vitro* (E) at the indicated DIVs (n = 4 MEAs). Data are normalized to the activity at 8 DIV. **F-J,** tdT-transfected 21 DIV MHNs in control (normoxia) conditions (F) or after 20 DIV in control conditions plus an additional 16 hrs in hypoxia (G), and analyzed for protrusion density (H), protrusion length (I) and percentage of spines with head (J) ($n \geq 7$ neurons, 12 dendrites, 350-500 protrusions). **K,** Quantification of apoptotic ($TUNEL^+$) 14 DIV MHNs after control, hypoxia or DMOG treatment for 16 hrs. **L,** Representative immunoblot (IB) for PARP1 and tubulin in lysates from 14 DIV MHN after control (normoxia), DMOG or hypoxia treatment for 16 hrs. Brain lysate (Bl) was used as positive control. Arrows indicate full-length (fl) or cleaved (cl) PARP1. **M,** Representative IB for active (act) caspase3 and tubulin in lysates from 14 DIV MHN after control (normoxia), DMOG or hypoxia treatment for 16 hrs. Brain lysate (Bl) was used as positive control. **N**, Content of oxidized glutathione (GSSG) vs. total glutathione (GSSG + GSH) (expressed in % of the value in normoxia) in 14 DIV MHNs in control normoxic conditions, hypoxia or DMOG treatment for 16 hrs. MHNs treated with 100 μM H_2O_2 for 1 hr were used as a positive control (H_2O_2). **O,** RT-PCR expression analysis of hypoxia-responsive genes in MHNs exposed to hypoxia or treated with DMOG for 16 hrs (expressed in % of normoxia control; n = 3 experiments). *Phd3*, prolyl hydroxylase domain 3; *Pdk1*, pyruvate dehydrogenase kinase 1; *Vegfa*, vascular endothelial growth factor A. **P,** Quantification of luciferase activity from MHNs transfected with the HIF-dependent luciferase reporter HRE::luc plasmid and incubated for the indicated time points in control (ctrl) conditions, DMOG (D) treatment or hypoxia (H) alone or combined with the HIF-inhibitor acriflavine (Ac). A.U., arbitrary units. Data are mean ± SEM. *$p < 0.05$, ***$p < 0.001$. Scale bar, 5 μm (F,G).

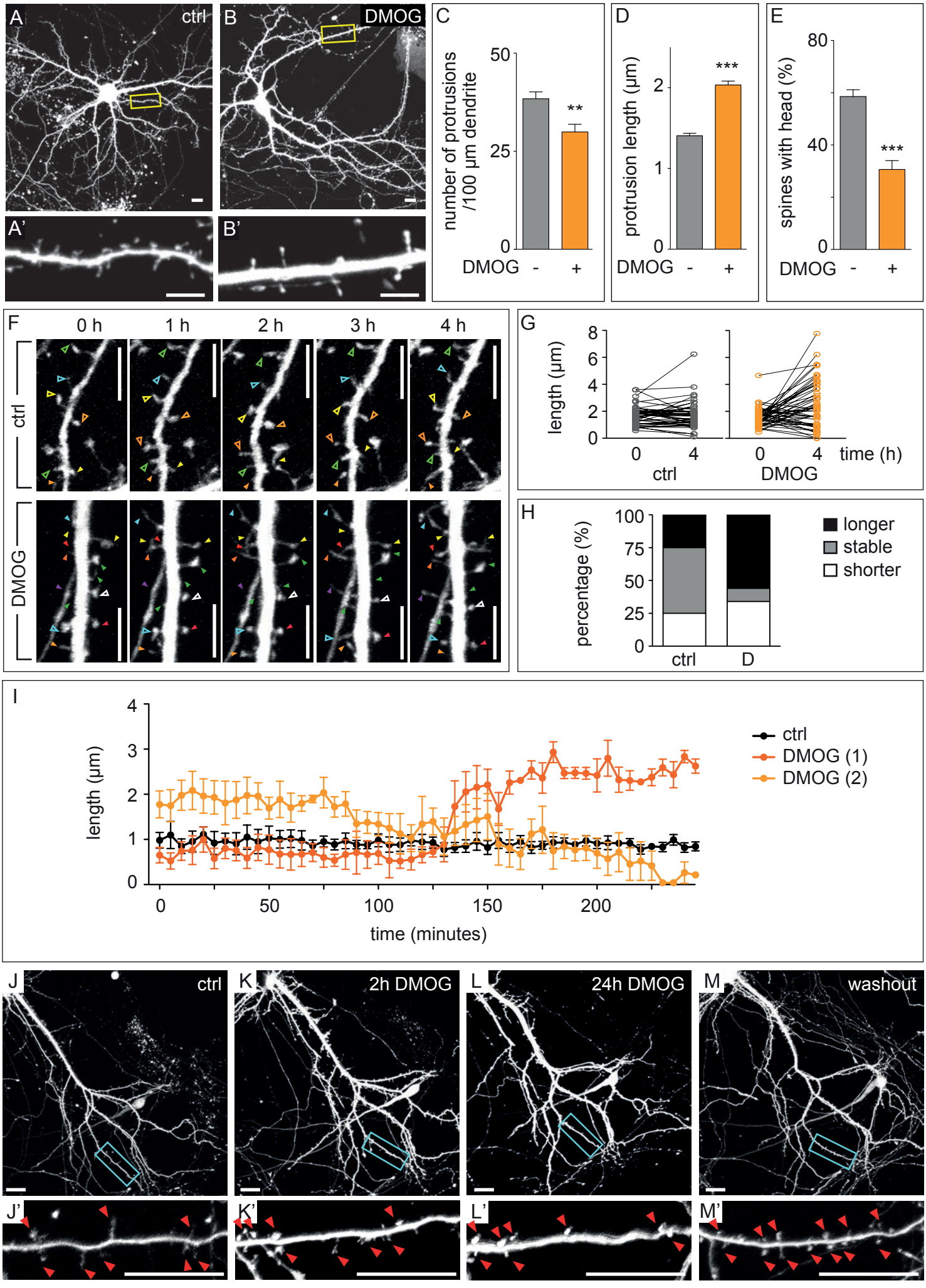
A
ctrl
B
DMOG
A'
B'
C
number of protrusions /100 µm dendrite
50
25
0
**
DMOG - +
D
protrusion length (µm)
2
1
0
***
DMOG - +
E
spines with head (%)
80
40
0
***
DMOG - +
F
0 h
1 h
2 h
3 h
4 h
ctrl
DMOG
G
length (µm)
8
6
4
2
0
0 4
ctrl
0 4
DMOG
time (h)
H
percentage (%)
100
75
50
25
0
ctrl
D
longer
stable
shorter
I
length (µm)
4
3
2
1
0
0
50
100
150
200
time (minutes)
ctrl
DMOG (1)
DMOG (2)
J
ctrl
K
2h DMOG
L
24h DMOG
M
washout
J'
K'
L'
M'

FIGURE S2

FIGURE S2; RELATED TO FIGURE 1

A-E, YFP-transfected MHNs were incubated for 16 hrs under control (A) or 250 μM DMOG (B) and analyzed for protrusion density (C), protrusion length (D) and percentage of spines with head (E) (n = 3 experiments, ≥ 21 neurons, > 550 protrusions). A'-B' show higher magnifications of the box in A or B. **F**, Snap-shot images at the start (0) and after 1, 2, 3 or 4 hrs of time-lapse recording of 14 DIV tdT-labeled MHNs, in control (upper) or DMOG conditions (lower). Solid arrowheads: spines with persistent increase or decrease in length; open arrowheads: spines that do not change their length. Each color denotes a distinct spine. **G,H**, Length of single protrusions at 0 and 4 hrs recording for control and DMOG (G; n ≥ 40) and distribution of spines according to length variation (H). Stable: Δ-length ≤ 0.2 μm..**I,** Diagram showing the average length of randomly selected control (black) and DMOG-treated (orange) dendritic spines over time, showing different subpopulations responding to the treatment by reducing (light orange) or increasing (dark orange) their length; n = 5 spines per condition; representative of 3 experiments. **J-M',** Representative pictures of the same tdT transfected MHN taken at 13 DIV before treatment (J,J'), at 14 DIV after DMOG treatment for 2 hrs (K,K'), at 15 DIV after DMOG treatment for 24 hrs (L,L'), and at 18 DIV after washout for 3 DIV (M,M'). J'-M' show higher magnification of the boxed areas in J-M; red arrowheads: dendritic protrusions. Data are mean ± SEM. **p < 0.01, ***p < 0.001. Scale bar, 5 μm (A',B',F), 10 μm (A,B), 20 μm (J, J'-M, M').

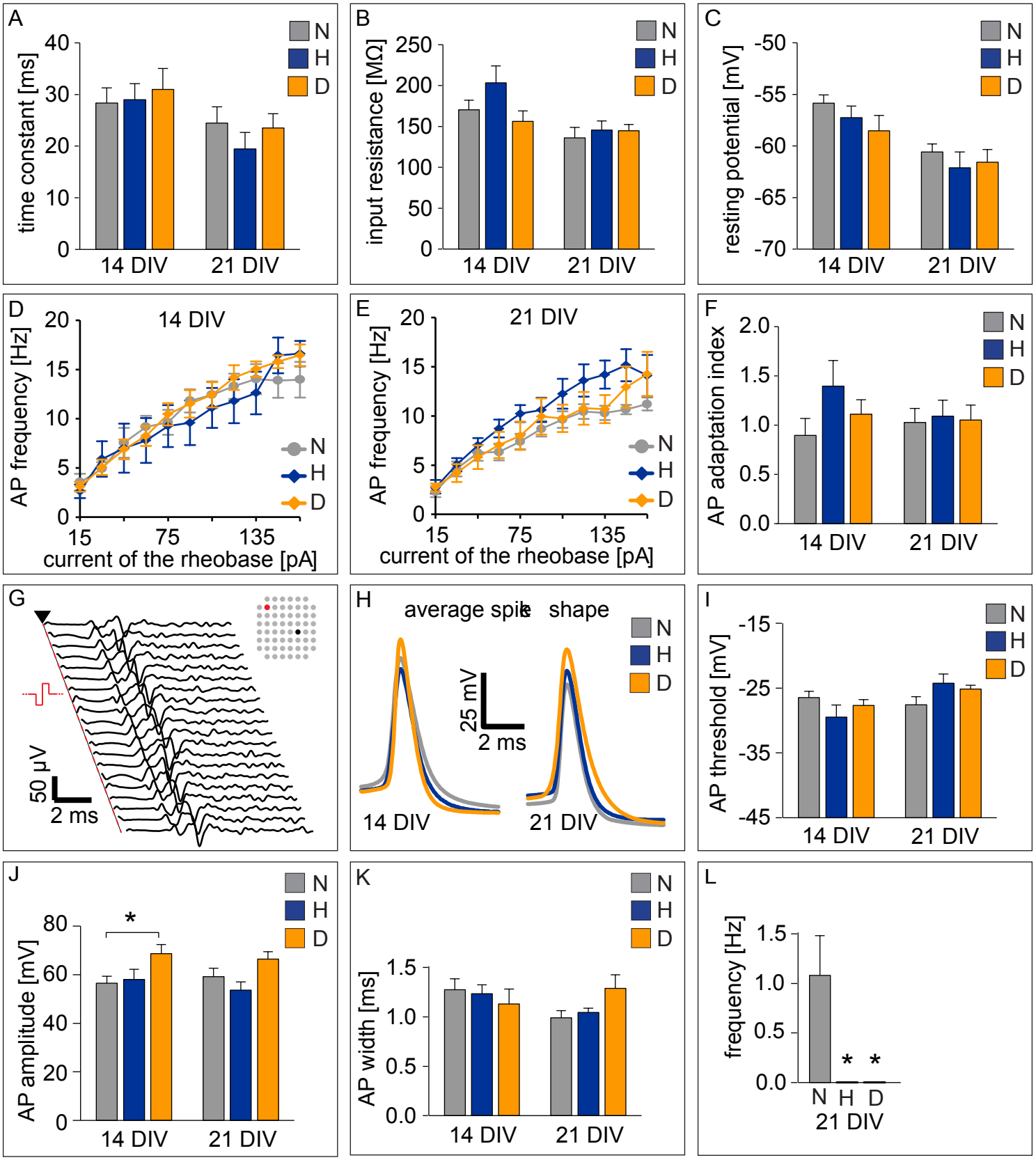
A
time constant [ms]
40
30
20
10
0
14 DIV
21 DIV
N
H
D
B
input resistance [MΩ]
250
200
150
100
50
0
C
resting potential [mV]
-50
-55
-60
-65
-70
D
14 DIV
AP frequency [Hz]
20
15
10
5
0
15
75
135
current of the rheobase [pA]
E
21 DIV
F
AP adaptation index
2.0
1.5
1.0
0.5
0.0
G
50 µV
2 ms
H
average spike shape
25 mV
2 ms
I
AP threshold [mV]
-15
-25
-35
-45
J
AP amplitude [mV]
80
60
40
20
0
*
K
AP width [ms]
1.5
1.0
0.5
0.0
L
frequency [Hz]
1.5
1.0
0.5
0.0
* *
N H D
21 DIV

FIGURE S3

FIGURE S3; RELATED TO FIGURE 2

In all panels, N: normoxia, H, hypoxia (1% O_2), D: DMOG (250 μM (A-F,H-L) or 1 mM (N,O)), H/N: hypoxia o/n followed by 24 hrs normoxia. **A-C,** Single-neuron passive electrical properties of 14 and 21 DIV MHNs, measured by patch-clamp at the soma (n = 30 neurons) and quantification of the membrane time constant (A), apparent input resistance (B), and membrane resting potential (C). **D-F,** Excitable, active electrical neuronal properties (n = 30 neurons) of 14 (D,F) and 21 DIV (E,F) MHNs, studied by the relationship between current amplitude of the rheobase and the mean frequency of evoked action potential (AP; D,E), and by the temporal adaptation of successive APs in a train (F). **G**, Antidromic APs could be elicited with no failures during hypoxia by 20 repeated extracellular electrical pulses (monopolar configuration, biphasic waves, 1 ms x 800 mV, negative phase first) delivered via substrate-integrated microelectrode arrays (MEAs). The inset sketches the MEA layout, with the stimulating microelectrode in red, and the recording microelectrode in black. The resulting traces were comparable to those obtained in normoxia (not shown) in their "all-or-none" quality, directly arising from the unaltered cellular and axonal excitability (see also panels D,E). **H**, Average spike shape of spontaneous APs, after recording non stop for 5 minutes and averaging all APs fired, in 14 or 21 DIV MHNs in the indicated conditions. **I-K**, Typical AP features of 14 and 21 DIV MHNs, including threshold (i.e., calculated as the first maximum of the third derivative of the membrane voltage during an AP; I), peak amplitude (J), and width (K). **L**, Spontaneous AP firing as recorded intracellularly by patch-clamp in 21 DIV MHNs, in the indicated conditions, shown as average frequency. **M**, Representative raster plots of the spiking activity, detected in the same neuronal culture by an array of 60 extracellular microelectrodes (MEAs), in normoxia, during hypoxia (after overnight treatment), and 24 hrs after return to normoxia. The spontaneous occurrence of one or more action potentials, detected at each of the 60 distinct microelectrode locations, is indicated by a black dot: prominent episodic synchronization is apparent from the vertical structures (i.e., bursts) in the plots and indirectly indicates functional glutamatergic synaptic transmission. **N,O**, Frequency of spontaneous AP firing (N) and spontaneous network-wide AP synchronization (O) (n = 4 MEAs/condition), for the indicated DIV and condition. **P-S,** MHN at 14 DIV transfected with YFP (green) and subjected at 20 DIV for 16 hrs to normoxia (P), hypoxia (Q) or 250 μM DMOG (R), fixed and stained for presynaptic synaptophysin (red). The red dots lying outside of the YFP^+ neuron are from neighbouring neurons. Quantification of synaptic density per dendritic length (by counting the yellow clusters and the red clusters in immediate apposition with the dendrite/spine) is shown in S ($n \geq 10$ neurons). Data are mean ± SEM. *$p < 0.05$, **$p < 0.01$, ***$p < 0.001$ (vs. normoxia ctrl). Scale bar, 2 mm (A, top panels), 1 mm (1, bottom panels), 5 μm (P-R).

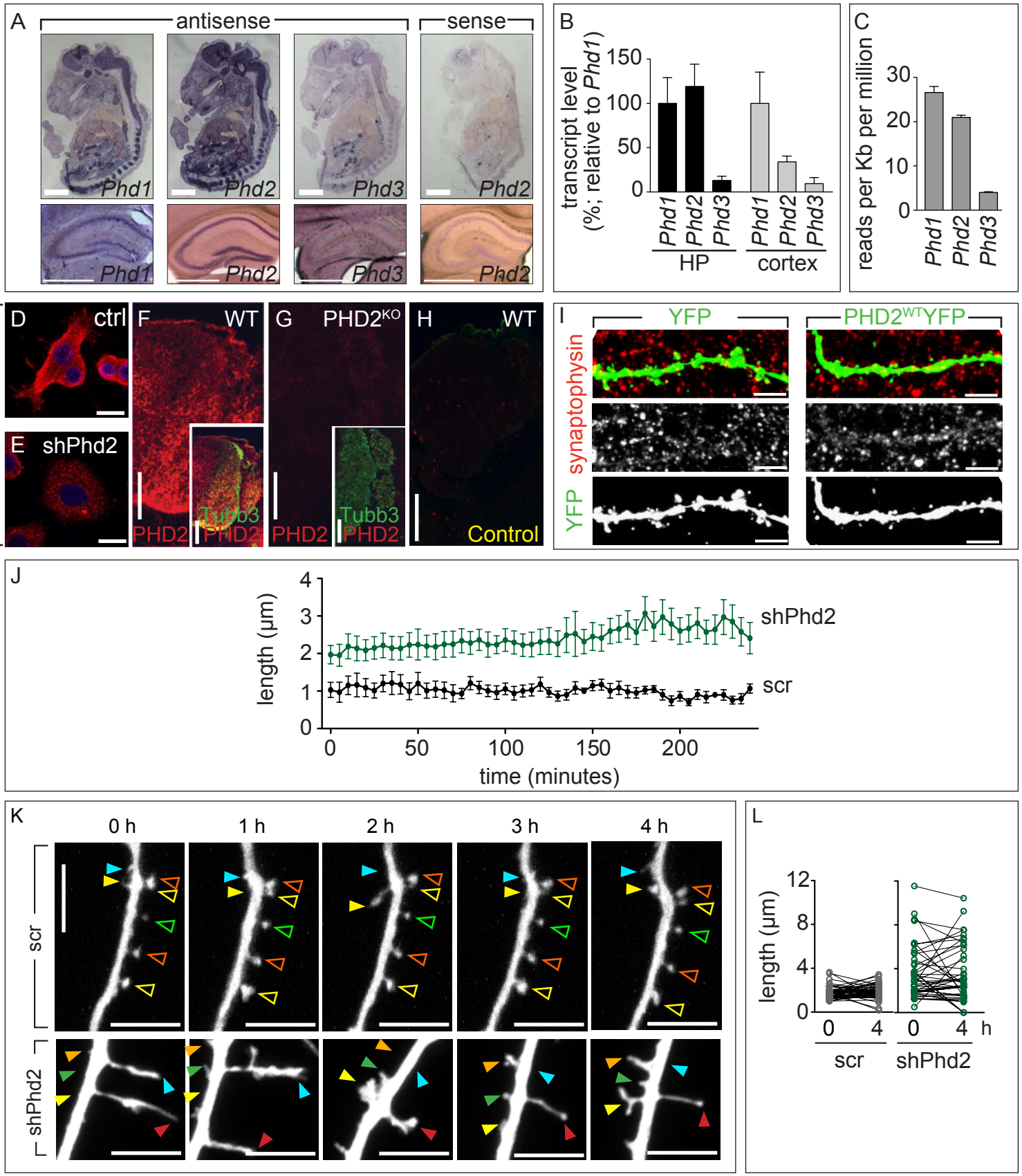
A
antisense
sense
Phd1
Phd2
Phd3
Phd2
B
transcript level
(%; relative to Phd1)
150
100
50
0
Phd1
Phd2
Phd3
Phd1
Phd2
Phd3
HP
cortex
C
reads per Kb per million
30
20
10
0
Phd1
Phd2
Phd3
PHD2
DAPI
D
ctrl
E
shPhd2
F
WT
Tubb3
PHD2
PHD2
G
PHD2KO
Tubb3
PHD2
PHD2
H
WT
Control
I
YFP
PHD2WTYFP
synaptophysin
YFP
J
length (µm)
4
3
2
1
0
shPhd2
scr
0
50
100
150
200
time (minutes)
K
0 h
1 h
2 h
3 h
4 h
scr
shPhd2
L
length (µm)
12
8
4
0
0
4
0
4
h
scr
shPhd2

FIGURE S4

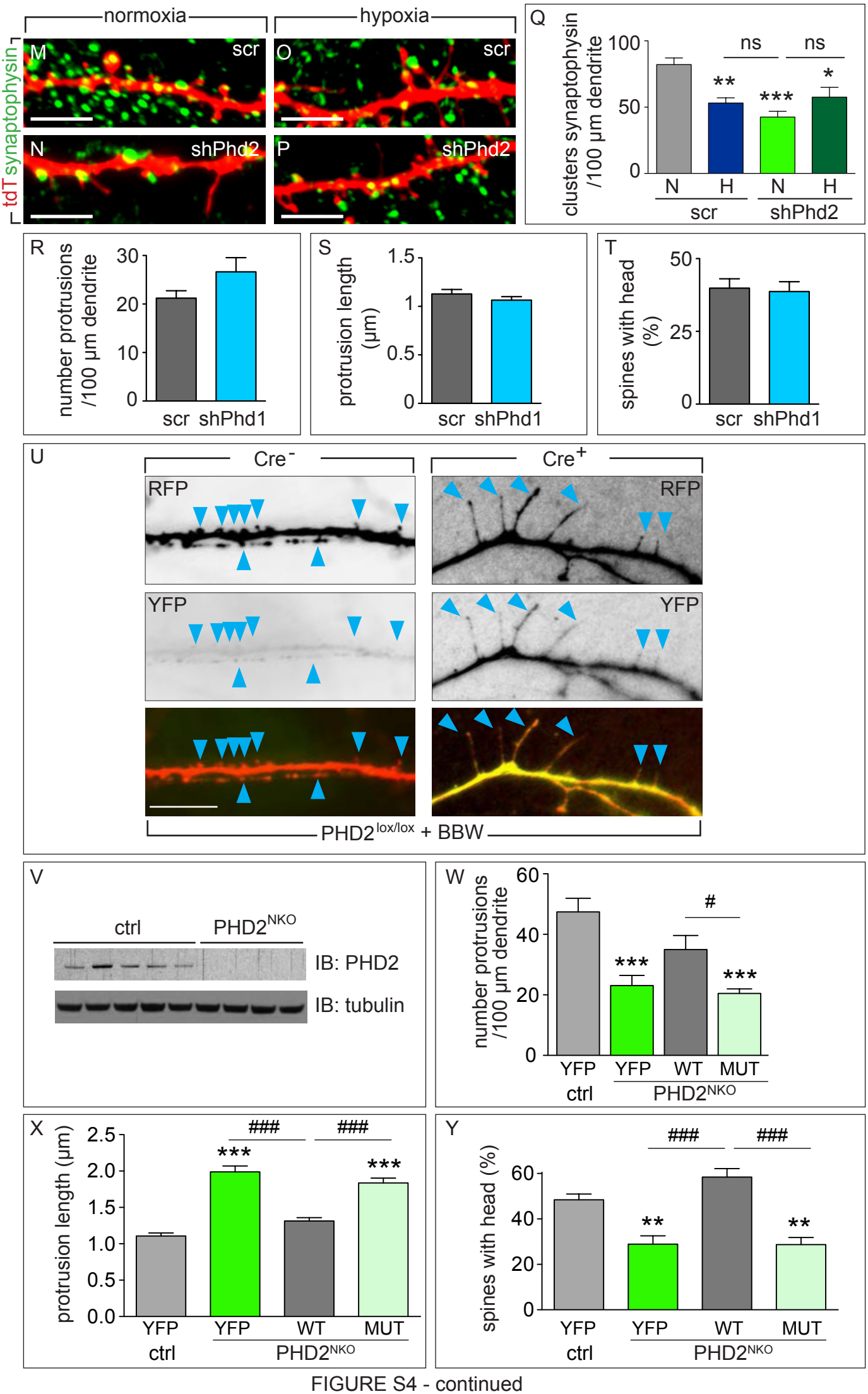

FIGURE S4 - continued

FIGURE S4; RELATED TO FIGURE 3

A, *In situ* hybridization with *Phd1 (also known as Egln2)*, *Phd2 (Egln2)* and *Phd3 (Egln3)* antisense probes or *Phd2* sense probe, in cryosections from E14.5 mouse embryos (upper panels) or in free-floating adult hippocampal coronal sections (lower panels). **B,** Relative mRNA expression of *Phd1*, *Phd2* and *Phd3* genes in E17 hippocampus (HP) and E14.5 cortex (n = 3 embryos). **C,** Quantitative mRNA expression of *Phd1*, *Phd2* and *Phd3* genes in 2 weeks old mouse brains by RNA-seq analysis (n = 3 mice). **D,E,** PC12 cells in control conditions (ctrl, D) or upon silencing of *Phd2* (shPhd2, E) and immunostained for PHD2 (red) and DAPI (blue), showing only negligible (background) staining upon *Phd2* silencing. **F-H,** Immunostaining for PHD2 (red) in cryosections from the trunk of E11.5 control (F) or $PHD2^{KO}$ littermates (G). Small insets show co-staining with the neuronal marker ßIII-tubulin (Tubb3, green). Control staining without both primary antibodies (H). **I,** Representative images of MHNs transfected with YFP or $PHD2^{WT}$YFP expression constructs (green in top panels; white in lower panels) and immunostained for synaptophysin (red in top panels; grayscale in middle panels), showing the expression pattern of $PHD2^{WT}$YFP in neurons in culture, including its presence in postsynaptic sites. The red dots lying outside of the YFP^{+} neuron are from neighbouring neurons. **J,** Diagram showing the average length of 5 representative scr (black) or shPhd2 (green) dendritic spines over time; representative of 3 experiments. **K,** Snap-shot images at the start (0) and after 1, 2, 3 or 4 hrs of time-lapse recording in normoxia of 14 DIV MHNs co-transfected with YFP or EGFP plus scrambled control shRNA (scr, upper panels) or shPhd2 (lower panels),. Solid arrowheads: spines with persistent increase or decrease in length (longer or shorter at 4 hrs, as compared to the start); open arrowheads: spines that do not change their length. Each color denotes a distinct spine. **L,** Length of single protrusions at 0 and 4 hrs recording for control and *Phd2* silenced neurons; $n \geq 45$ spines. **M-Q,** MHNs were co-transfected at 14 DIV with tdT (red) and with either scr (M,O) or shPhd2 (N,P), subjected at 20 DIV for 16 hrs to normoxia (M,N) or hypoxia (1% O_2, O,P) and stained for synaptophysin (green). The green dots lying outside of the tdT^{+} neuron are from neighbouring neurons. Quantification of synaptic density per dendritic length (yellow clusters and green clusters in immediate apposition with the dendrite/spine) is shown in panel Q (n = 8-14 neurons). **R-T,** Quantification of protrusion density (R), protrusion length (S) and percentage of spines with head (T) of MHNs transfected with scr or shPhd1 ($n \geq 10$ neurons, 14-15 dendrites, >200 protrusions). **U,** MHNs isolated from $Phd2^{lox/lox}$ E16.5 embryos were transfected with the Brainbow1.0 plasmid (BBW) alone (Cre^{-}) or combined with a Cre-recombinase expressing plasmid (Cre^{+}) at 7 DIV, and imaged at 14 DIV. Note that the Cre^{-} MHN expresses only RFP, while the Cre^{+} MHN expresses YFP and residual RFP. Arrowheads: dendritic protrusions. **V,** Representative IB for PHD2 and tubulin of homogenates obtained from the hippocampus of control (ctrl) and $PHD2^{NKO}$ littermates. **W-Y,** Quantification of protrusion density (W), protrusion length (X) and percentage of spines with head (Y) of 14 DIV MHN isolated from ctrl or $PHD2^{NKO}$ littermates upon transfection at 7 DIV with YFP, $PHD2^{WT}$YFP (WT) or $PHD2^{MUT}$YFP (MUT)). Corresponding representative images are shown in Fig. 3S (n = 7-15 neurons, 203-335 protrusions). Data are mean ± SEM; ns = not significant, $*p < 0.05$, $**p < 0.01$, $***p < 0.001$ vs. scr control in normoxia (Q) or vs. ctr (W-Y); $\#p < 0.01$, $\#\#\#p < 0.001$ between indicated bars. Scale bar: 10 μm (D,E), 5 μm (I,K,M-O,U), 100 μm (F-H).

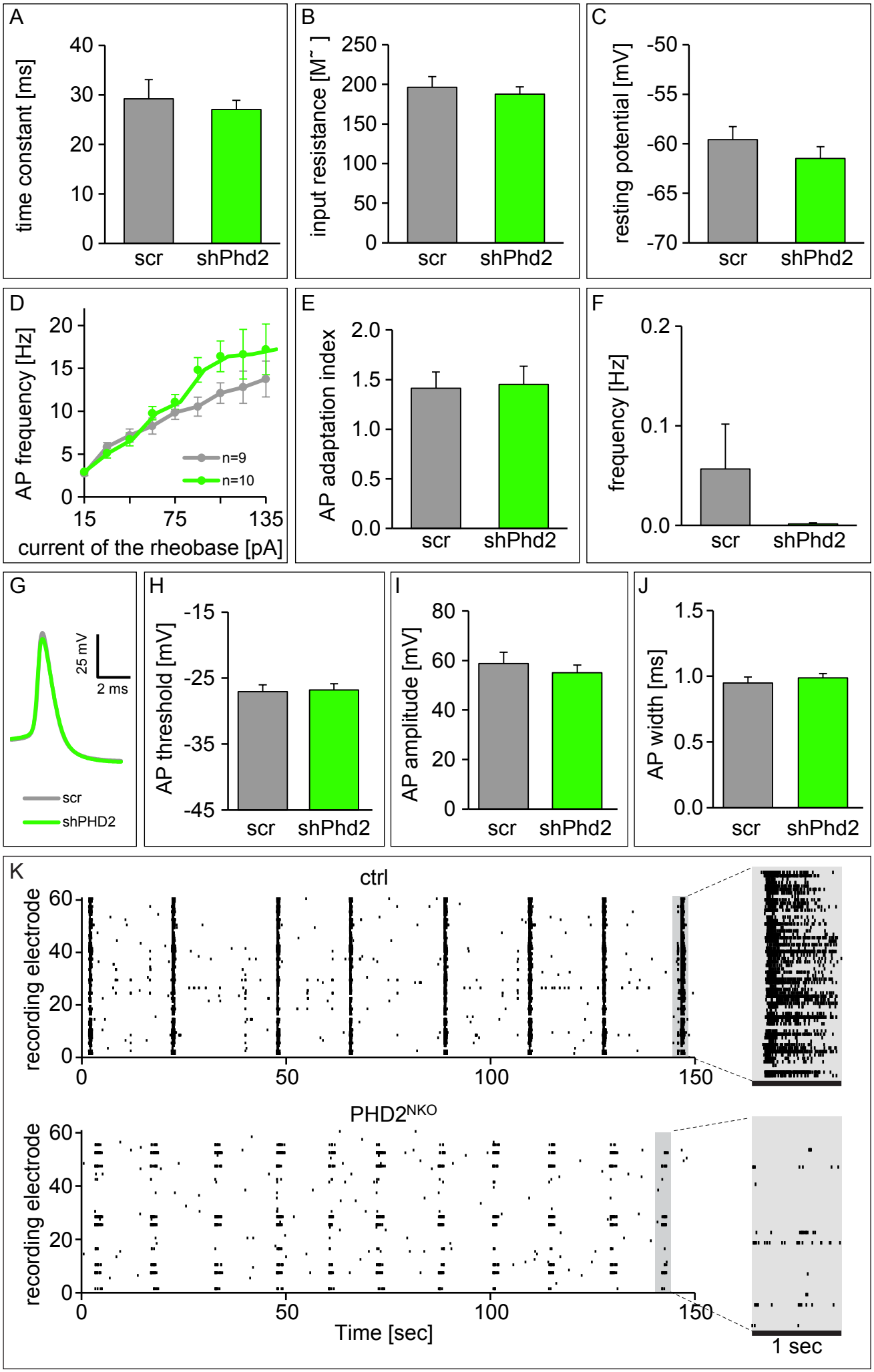
A
time constant [ms]
40
30
20
10
0
scr
shPhd2
B
input resistance [M˜]
250
200
150
100
50
0
scr
shPhd2
C
resting potential [mV]
-50
-55
-60
-65
-70
scr
shPhd2
D
AP frequency [Hz]
20
15
10
5
0
n=9
n=10
15
75
135
current of the rheobase [pA]
E
AP adaptation index
2.0
1.5
1.0
0.5
0.0
scr
shPhd2
F
frequency [Hz]
0.2
0.1
0.0
scr
shPhd2
G
25 mV
2 ms
scr
shPHD2
H
AP threshold [mV]
-15
-25
-35
-45
scr
shPhd2
I
AP amplitude [mV]
80
60
40
20
0
scr
shPhd2
J
AP width [ms]
1.5
1.0
0.5
0.0
scr
shPhd2
K
ctrl
recording electrode
60
40
20
0
0
50
100
150
PHD2NKO
recording electrode
60
40
20
0
0
50
100
150
Time [sec]
1 sec

FIGURE S5

FIGURE S5; RELATED TO FIGURE 3

A-C, Single-cell passive membrane properties (membrane time constant (A), input resistance (B) and membrane resting potential (C)) measured from soma using patch-clamp recordings in MHNs transduced with lentiviral vectors expressing scrambled (scr) or shPhd2 (n = 27 neurons). **D,E,** Active electrical neuronal properties estimated by mean frequency of evoked action potential in response to current steps with increasing amplitude (D) and time adaptation of action potentials (E) in MHNs transduced with lentiviral vectors expressing scr or shPhd2 (n = 9-10 neurons). **F,** Network properties characterized by the frequency of spontaneous action potentials in MHNs transduced with lentiviral vectors expressing scr or shPhd2 (n = 9-10 neurons). **G-J,** Single action potential properties represented by average shape of action potentials (G), threshold (H), amplitude (I) and width (J), in MHNs transduced with lentiviral vectors expressing scr or shPhd2 (n = 9-10 neurons in H-J). **K**, Representative raster plots of the spiking activity at 14 DIV, detected in two MEAs each obtained from a set of control (top) or $PHD2^{NKO}$ neurons (bottom). The spontaneous occurrence of action potentials detected by each of the 60 distinct microelectrodes is indicated by a black dot. Prominent episodic synchronization is apparent in control but not in $PHD2^{NKO}$ cultures. The insets highlight the differences in the firing of the two neuronal networks at higher temporal resolution. Data are mean ± SEM.

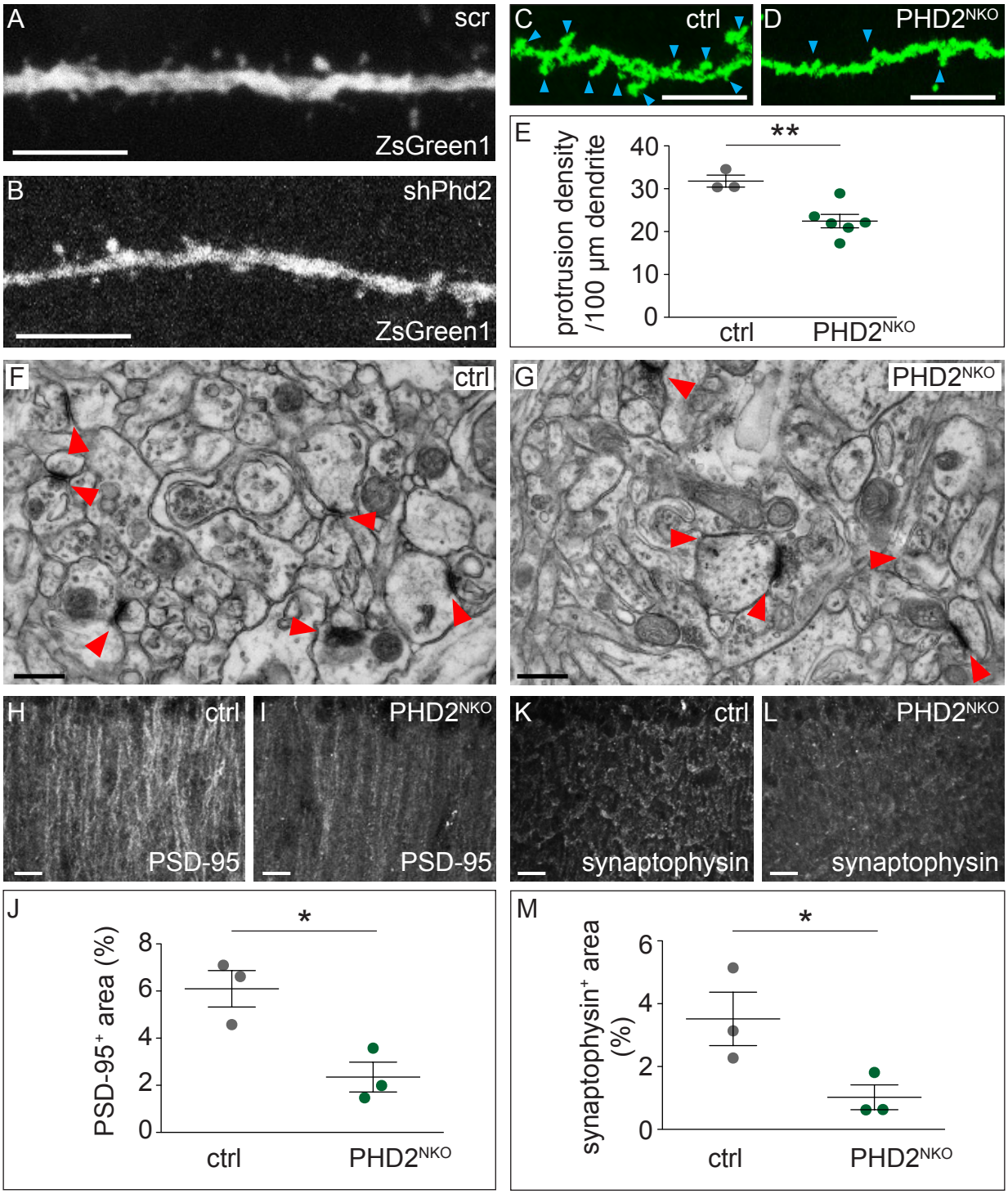
A
scr
ZsGreen1
B
shPhd2
ZsGreen1
C
ctrl
D
PHD2NKO
E
protrusion density /100 µm dendrite
40
30
20
10
0
**
ctrl
PHD2NKO
F
ctrl
G
PHD2NKO
H
ctrl
PSD-95
I
PHD2NKO
PSD-95
K
ctrl
synaptophysin
L
PHD2NKO
synaptophysin
J
PSD-95+ area (%)
8
6
4
2
0
*
ctrl
PHD2NKO
M
synaptophysin+ area (%)
6
4
2
0
*
ctrl
PHD2NKO

FIGURE S6

FIGURE S6; RELATED TO FIGURE 3

A,B, Representative ZsGreen1^{+} dendritic segments from the CA1 region of hippocampal slices of 2-weeks old WT mice that were *in utero* electroporated at E15.5 with a scrambled control shRNA (scr) (A) or shPhd2 (B). **C-E,** Representative dendritic segments from hippocampi of 2 weeks old control (ctrl; C) or PHD2^{NKO} (D) mice, detected by using the Golgi impregnation imaged under the reflection mode of the microscope. Arrowheads: dendritic spines. Panel E shows the quantification of the dendritic protrusion density (n = 3-6 animals). **F,G,** Representative images of the *stratum radiatum* of the CA1 hippocampal region of ctrl (F) or PHD2^{NKO} (G) mice obtained by transmission electron microscopy. Red arrowheads: post-synaptic densities (n = 3-4 animals). **H-M,** Representative images of anti-PSD-95 staining (H,I) and anti-synaptophysin staining (K,L) of the *stratum radiatum* of the CA1 hippocampal region of control (ctrl; H,K) or PHD2^{NKO} (I,L) mice. Quantification of PSD-95^{+} area (panel J; n = 3) and synaptophysin^{+} area (panel M; n = 3) (after setting a common intensity threshold). Single data plus mean ± SEM are shown. *$p < 0.05$, **$p < 0.01$. Scale bar, 5 μm (A,B), 10 μm (C,D), 500 nm (F,G), 20 μm (H,I,.K,L).

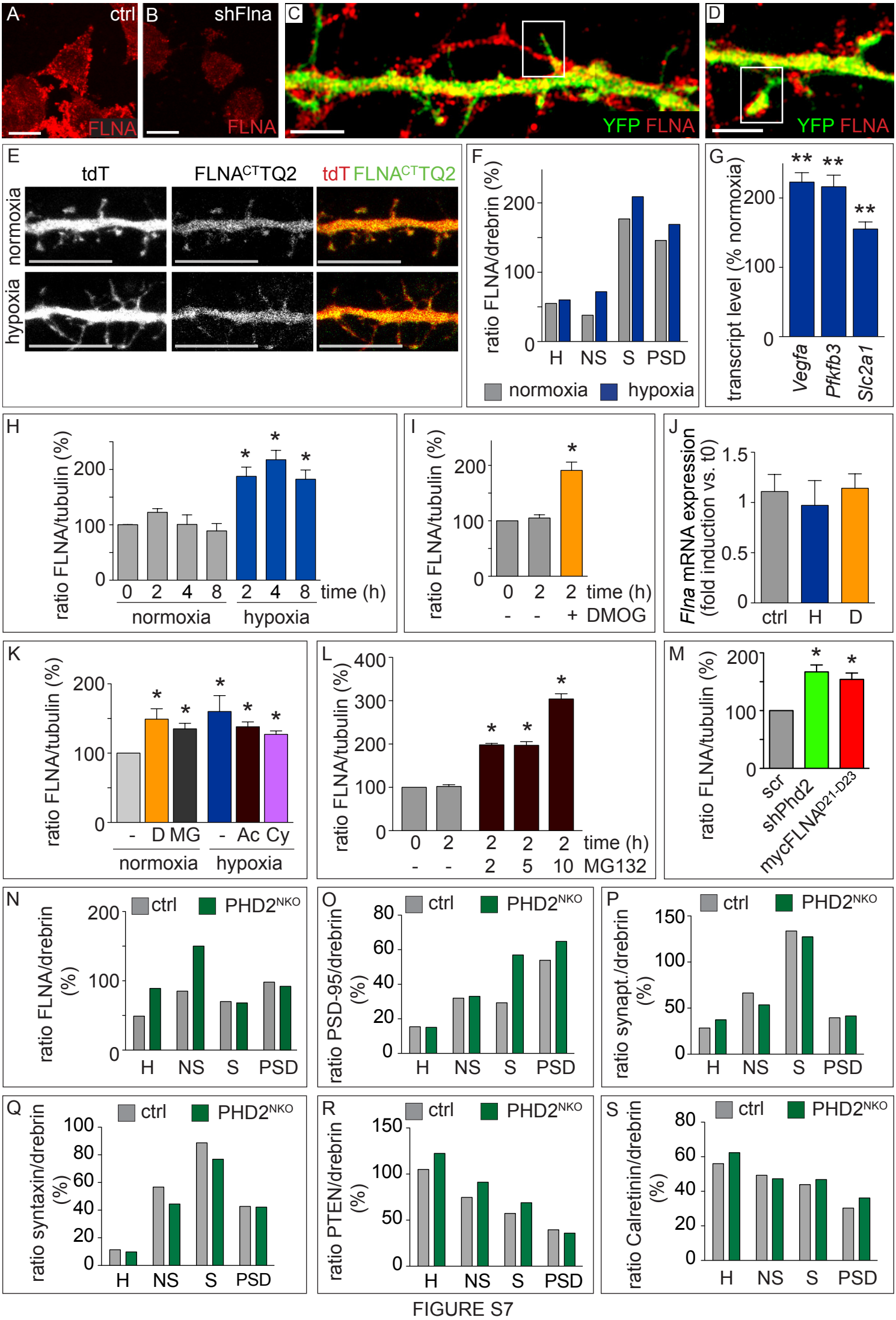
A
ctrl
FLNA
B
shFlna
FLNA
C
YFP FLNA
D
YFP FLNA
E
tdT
FLNA^CTTQ2
tdT FLNA^CTTQ2
normoxia
hypoxia
F
ratio FLNA/drebrin (%)
200
100
0
H NS S PSD
normoxia
hypoxia
G
transcript level (% normoxia)
200
100
0
**
**
**
Vegfa
Pfkfb3
Slc2a1
H
ratio FLNA/tubulin (%)
200
100
0
*
*
*
0 2 4 8 2 4 8 time (h)
normoxia
hypoxia
I
ratio FLNA/tubulin (%)
200
100
0
*
0 2 2 time (h)
- - + DMOG
J
Flna mRNA expression
(fold induction vs. t0)
1.5
1
0.5
0
ctrl H D
K
ratio FLNA/tubulin (%)
200
100
0
*
*
*
*
*
- D MG - Ac Cy
normoxia
hypoxia
L
ratio FLNA/tubulin (%)
400
300
200
100
0
*
*
*
0 2 2 2 2 time (h)
- - 2 5 10 MG132
M
ratio FLNA/tubulin (%)
200
100
0
*
*
scr
shPhd2
mycFLNA^D21-D23
N
ratio FLNA/drebrin (%)
ctrl
PHD2^NKO
200
100
0
H NS S PSD
O
ratio PSD-95/drebrin (%)
ctrl
PHD2^NKO
80
60
40
20
0
H NS S PSD
P
ratio synapt./drebrin (%)
ctrl
PHD2^NKO
150
100
50
0
H NS S PSD
Q
ratio syntaxin/drebrin (%)
ctrl
PHD2^NKO
100
80
60
40
20
0
H NS S PSD
R
ratio PTEN/drebrin (%)
ctrl
PHD2^NKO
150
100
50
0
H NS S PSD
S
ratio Calretinin/drebrin (%)
ctrl
PHD2^NKO
80
60
40
20
0
H NS S PSD

FIGURE S7

FIGURE S7; RELATED TO FIGURE 4

A,B, PC12 cells in control conditions (ctrl, A) or after silencing of *Flna* (shFlna, B), and immunostained for FLNA (red). **C,D,** Representative images of YFP transfected RHNs immunostained for endogenous FLNA (red). Boxes denote regions that are shown at higher magnification in Fig. 4A. **E,** 14 DIV MHNs co-transfected with tdT (red) and C-terminus FLNA-TQ2 ($FLNA^{CT}TQ2$, green) incubated in normoxia (top) or hypoxia (bottom) for 16 hrs. Left and middle panels: single tdT or $FLNA^{CT}TQ2$ signal channel, respectively, in gray scale. The right panels: merged images. **F,** Densitometric quantifications of the ratio of FLNA protein levels (normalized to drebrin) of the immunoblot (IB) shown in Fig. 4C. **G,** Quantification of mRNA transcripts of HIF-target genes. Two weeks old mice were maintained under normal atmospheric conditions or exposed to hypoxia (8% O_2) for 4-5 hrs before sacrifice. mRNA was isolated from the brains and quantified by RNA-Seq (n = 3 mice). *Vegfa*, vascular endothelial growth factor A; *Pfkfb3*, phosphofructokinase-2/fructose-2,6-bisphosphatase 3; *Slc2a1*, solute carrier family 2 (facilitated glucose transporter) member 1 (Glut1). **H**, Densitometric quantification of FLNA IBs from 14 DIV MHNs incubated under hypoxia for the indicated time points (expressed in % of the value at 0 hrs in normoxia, n = 5). A representative blot is shown in Fig. 4D. **I**, Densitometric quantification of FLNA IBs from 14 DIV MHNs treated for 2 hrs without or with DMOG (n = 4). A representative blot is shown in Fig. 4E. **J,** Quantification of *Flna* transcript levels in MHNs under control (ctrl), hypoxia (H) or DMOG (D) treatment for 4 hrs, normalized to the value at 0 hrs (n = 3). **K**, Densitometric quantification of FLNA IBs from homogenates of MHNs in normoxia or hypoxia in the absence (-) or presence of DMOG (D), MG132 (MG), actinomycin D (Ac) or cycloheximide (Cy) (expressed in % of the value in untreated MHNs in normoxia, n = 3). A representative blot is shown in Fig. 4F. **L**, Densitometric quantification of FLNA IBs from homogenates of MHNs treated for 2 hrs with increasing concentrations of MG132 (expressed in % of the value in untreated MHNs at 0 hrs, n = 3). A representative blot is shown in Fig. 4G. **M**, Densitometric quantifications of FLNA IBs from homogenates of MHNs transduced with scr, shPhd2 or overexpressing myc-tagged FLNA deletion mutant D21-D23 ($mycFLNA^{D21\text{-}D23}$) (n = 3). A representative blot is shown in Fig. 4H. **N-S,** Densitometric quantifications of the levels of FLNA (N), the postsynaptic marker PSD-95 (O), the presynaptic markers synaptophysin (P) and syntaxin (Q) and of soluble fraction enriched markers PTEN (R) and calretinin (S) in mouse brain homogenate (H), non-synaptic fraction (NS), synaptic membranes (S) and PSD subfractions obtained from control (ctrl) or $PHD2^{NKO}$ littermates, as shown in the IBs in Fig. 4I. Data are mean ± SEM. *$p < 0.05$, **$p < 0.01$. Scale bar, 10 μm (A,B,E), 2 μm (C,D).

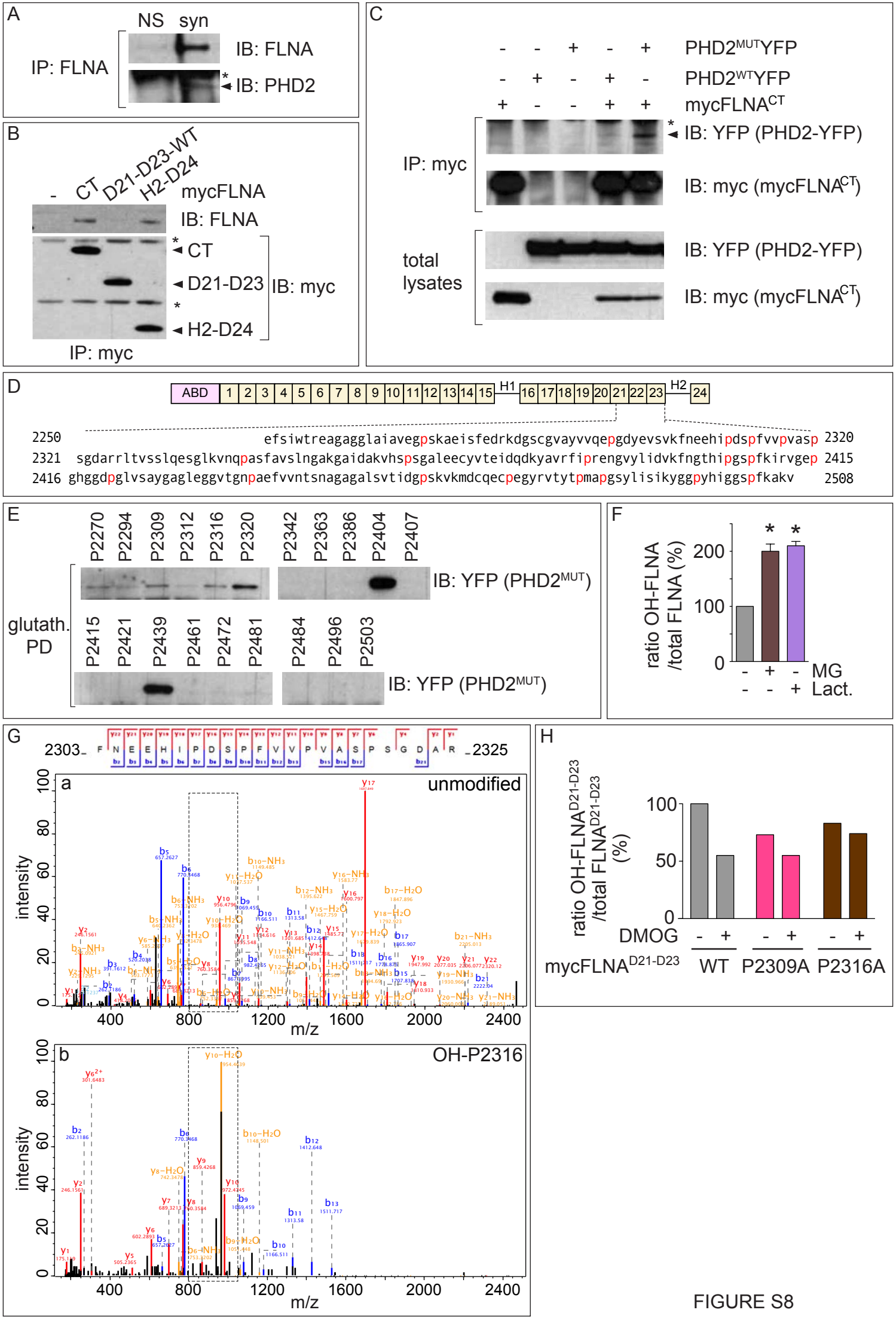
A
NS syn
IP: FLNA
IB: FLNA
IB: PHD2
B
- CT D21-D23-WT H2-D24 mycFLNA
IB: FLNA
CT
D21-D23
H2-D24
IB: myc
IP: myc
C
PHD2MUTYFP
PHD2WTYFP
mycFLNACT
IB: YFP (PHD2-YFP)
IP: myc
IB: myc (mycFLNACT)
total lysates
IB: YFP (PHD2-YFP)
IB: myc (mycFLNACT)
D
ABD
H1
H2
2250 efsiwtreagagglaiavegpskaeisfedrkdgscgvayvvqepgdyevsvkfneehipdspfvvpvasp 2320
2321 sgdarrltvsslqesglkvnqpasfavslngakgaidakvhspsgaleecyvteidqdkyavrfiprengvylidvkfngthipgspfkirvgep 2415
2416 ghggdpglvsaygagleggvtgnpaefvvntsnagagalsvtidgpskvkmdcqecpegyrvtytpmapgsylisikyggpyhiggspfkakv 2508
E
P2270 P2294 P2309 P2312 P2316 P2320 P2342 P2363 P2386 P2404 P2407
IB: YFP (PHD2MUT)
glutath. PD
P2415 P2421 P2439 P2461 P2472 P2481 P2484 P2496 P2503
IB: YFP (PHD2MUT)
F
ratio OH-FLNA /total FLNA (%)
MG
Lact.
G
2303_ F N E E H I P D S P F V V P V A S P S G D A R _2325
a unmodified
intensity
m/z
b OH-P2316
H
ratio OH-FLNAD21-D23 /total FLNAD21-D23 (%)
DMOG
mycFLNAD21-D23
WT P2309A P2316A

FIGURE S8

FIGURE S8; RELATED TO FIGURE 5

A, Representative IB for FLNA and PHD2 after immunoprecipitation (IP) of FLNA from non-synaptic (NS) and synaptic membrane (syn) subfractions of the brain of 2 weeks old mice. Arrow indicates PHD2, asterisk indicates the heavy chain of the IgGs used for the IP. **B,** Representative IB for myc and FLNA after IP of myc from HEK293T cells expressing myc-tagged FLNA deletion mutants mycFLNA^{CT} (CT), mycFLNA$^{D21\text{-}D23\text{-}WT}$ (D21-D23) or mycFLNA$^{H2\text{-}D24}$ (H2-D24). Arrows indicate the myc-tagged deletion mutants; asterisks indicate the heavy and light chains of the IgGs used for the IP. **C,** Representative IB for myc and YFP after IP of myc from HEK293T cells expressing mycFLNA^{CT}, PHD2^{WT}YFP or PHD2^{MUT}YFP alone or a combination of them. Arrow indicates the PHD2 after the IP; asterisk indicates aspecific band. Total lysate controls are shown (bottom). **D,** Amino acid sequence of the D21-D23 deletion mutant of FLNA that interacts with PHD2. Each line corresponds to the sequence of the different domains. The proline residues are indicated in red. **E,** Recombinant GST-fusion peptides, each containing a proline residue in FLNA$^{D21\text{-}D23\text{-}WT}$ (flanked by 6 amino acids upstream and downstream of the respective proline residue), were incubated with homogenates of HEK293T cells expressing PHD2^{MUT}YFP. Glutathione-beads were used to pull-down the complexes, and bound PHD2^{MUT}YFP was identified by IB for YFP. **F,** Densitometric quantification of hydroxyl-FLNA level in HEK293T cells transfected with myc-FLNA and treated for 2 hrs with MG132 (MG) or lactacystin (Lact.) (n = 3). A representative IB is shown in Fig. 5E. **G**, MS/MS fragmentation spectra of the unmodified (a) and hydroxylated P2316 (b; OH-P2316) sequence FNEEHIPDSPFVVPVASPSGDAR of FLNA. The boxed areas comprising the peaks corresponding to the proline P2316 containing fragments y10 are shown at larger scale in Fig. 5G. **H,** Densitometric quantification of the ratio hydroxylated/total mycFLNA$^{D21\text{-}D23}$ protein levels of IB from homogenates of HEK293T cells co-transfected with PHD2^{WT}YFP together with mycFLNA$^{D21\text{-}D23\text{-}WT}$, mycFLNA$^{D21\text{-}D23\text{-}P2309A}$ or mycFLNA$^{D21\text{-}D23\text{-}P2316A}$ in the absence or the presence of DMOG. The corresponding blot is shown in Fig. 5H. Data are mean ± SEM. *$p < 0.05$.

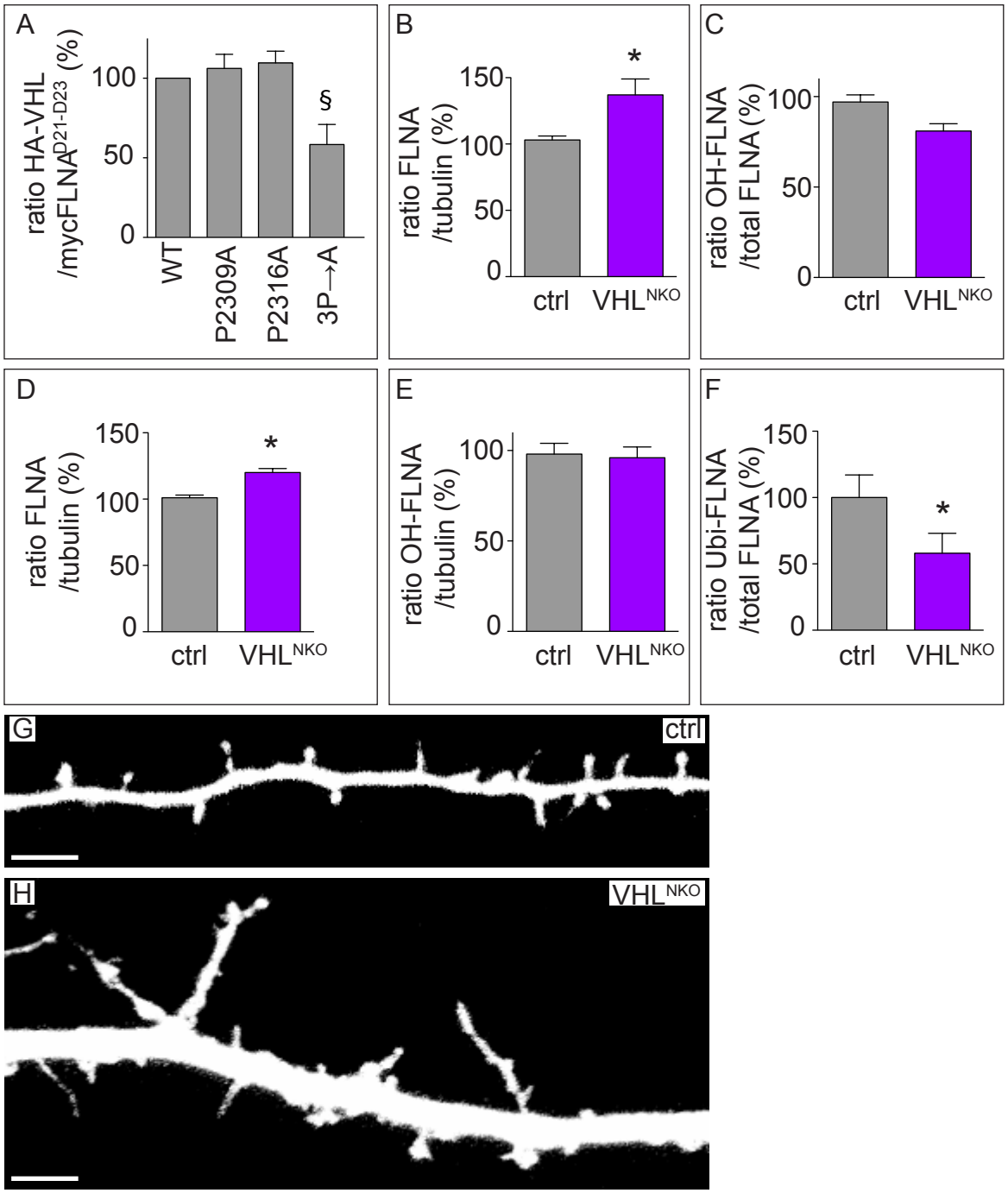
A
ratio HA-VHL /mycFLNA$^{D21-D23}$ (%)
100
50
0
§
WT
P2309A
P2316A
3P→A
B
ratio FLNA /tubulin (%)
150
100
50
0
*
ctrl
VHL^{NKO}
C
ratio OH-FLNA /total FLNA (%)
100
50
0
ctrl
VHL^{NKO}
D
ratio FLNA /tubulin (%)
150
100
50
0
*
ctrl
VHL^{NKO}
E
ratio OH-FLNA /tubulin (%)
100
50
0
ctrl
VHL^{NKO}
F
ratio Ubi-FLNA /total FLNA (%)
150
100
50
0
*
ctrl
VHL^{NKO}
G
ctrl
H
VHL^{NKO}

FIGURE S9

FIGURE S9; RELATED TO FIGURE 6

A, Densitometric quantification of the ratio of interaction between HA-VHL with wild type (WT) or mutant mycFLNA$^{D21-D23}$ (P2309A, P2316A or P2309/2312/2316A (3P→A)) (n = 3). A representative immunoblot (IB) is shown in Fig. 6C. **B**, Densitometric quantification of FLNA levels in brain homogenates obtained from E14.5 control (ctrl) or VHL^{NKO} littermates (n = 3-4 mice). The corresponding IB is shown in Fig. 6E. **C-E,** Densitometric quantification of the ratio of hydroxylated FLNA over total FLNA (C), FLNA protein level (D) or total hydroxyl-FLNA level (normalized to tubulin) (E) in brain homogenates obtained from E14.5 control (ctrl) or VHL^{NKO} littermates (n = 3-4 mice). The corresponding IB is shown in Fig. 6F. **F,** Densitometric quantification of the ubiquitinated-FLNA/total FLNA ratio in brain homogenates obtained from E14.5 control (ctrl) or VHL^{NKO} littermates and subjected to TUBE2 pull-down. The corresponding IB is shown in Fig. 6G (n = 2 mice). **G,H,** Representative images of 14 DIV MHNs from control (ctrl, G) or VHL^{NKO} (H) littermates and transfected with tdT. Data are mean ± SEM. * $p < 0.05$; § $p = 0.07$. Scale bar, 10 μm (G,H).

SUPPLEMENTAL EXPERIMENTAL PROCEDURES

ANIMALS

Animal housing and experimental procedures were approved by the Animal Ethics Committee of the KU Leuven (Belgium). *Wild type* (WT) Swiss mice and Wistar rats were used. *Phd2*$^{lox/lox}$ (Mazzone et al., 2009), PHD2-KO (Mazzone et al., 2009) and *Nestin*Cre (Tronche et al., 1999) mice had C57BL6 background. *Vhl*$^{lox/lox}$ (Haase et al., 2001) and *Hif-1α*$^{lox/lox}$ (Ryan et al., 2000) mice had BALB/c-C57BL6 mixed background.

MHN ISOLATION, CELL CULTURE, TRANSFECTION AND TRANSDUCTION

MOUSE AND RAT HIPPOCAMPAL NEURONS were isolated as previously described (Segura et al., 2007), and plated on coverslips or tissue culture plates coated with 0.2 mg/ml poly-D-lysine (Sigma) and 5 µg/ml laminin (Life Technologies). For the washout experiments, neurons were plated on culture plates marked with a grid (500 µm grid distance; IBIDI). Neurons were cultured in neurobasal medium supplemented with 1X B27 and 0.5 mM glutamine (all from Life Technologies). The neuronal density was 50-70,000 neurons per 24-well plate or 500,000 neurons per p35-dish (equivalent to 325-450 cells/mm^2). For *in vitro* electrophysiological experiments, cells were seeded on conventional glass coverslips or on substrate-integrated microelectrode arrays at a density of 1,000 cells/mm^2 or 3,200 cells/mm^2, respectively. Neurons were grown for 7-14 days in vitro (DIV) and transfected with Lipofectamine2000 (Life Technologies) following the manufacturer's instructions, and analyzed at 14 or 21 DIV. When indicated, 3-5 DIV neurons were transduced overnight (o/n) using 10 MOI lentiviral particles. For adenoviral particles, isolated MHN were incubated with 10 MOI particles for 15 min before plating. *HUMAN EMBRYONIC KIDNEY (HEK) 293T CELLS* were maintained in Dulbecco Modified Earl Media (DMEM) supplemented with 10% fetal bovine serum (FBS), 2 mM glutamine, 100 U/ml penicillin and 10 µg/ml streptomycin (all from Life Technologies). HEK293T cells were transfected by the calcium phosphate precipitation method. When indicated, cells were treated with the following concentrations of compounds: 250 µM DMOG (Enzo Life Sciences), 10 µM MG132 (Calbiochem), 10 µM lactacystin (Millipore), 5 µM acriflavine (Sigma), 1 µg/ml actinomycin D (Sigma), 20 µg/ml cycloheximide (Sigma). *RAT PC12 CELLS* were maintained in DMEM supplemented with 5% FBS, 5% horse serum, 2 mM glutamine, 100 U/ml penicillin and 10 µg/ml streptomycin (all from Life Technologies). PC12 cells were transfected with siRNA sequences for either rat PHD2 or FLNA (IDT Trifect) by nucleofection, program U29 (AMAXA). Cells were routinely maintained in culture at 37ºC, 5% CO_2 and 21% O_2. Hypoxic incubations were made in a 94% N_2, 5% CO_2, 1% O_2 atmosphere for neurons, and 94.8% N_2, 5% CO_2, 0.2% O_2 for HEK293T cells.

MORPHOGENESIS OF DENDRITIC SPINES IN NORMOXIA

To characterize dendritic spines *in vitro*, we first monitored the maturation of dendritic spines in monocultures of mouse hippocampal neurons (MHNs) during 21 days *in vitro* (DIV). To visualize single dendritic protrusions, we transfected 6 DIV MHNs with yellow fluorescent protein (YFP), enhanced green fluorescent protein (EGFP) or tandem dimer tomato (tdT) fluorescent protein. At 8 DIV, MHNs extend few, long immature dendritic protrusions (Fig. S1A-C). Three days later, more numerous dendritic protrusions extended from dendrites (Fig. S1A) and progressively matured over time towards shorter mushroom-shaped spines at 15 DIV (Fig. S1A-C). Beyond 16 DIV, dendritic spine density and maturation were maintained (not shown).

To determine whether the morphological analysis of dendritic spine maturation correlated with neuronal activity, we used multi-electrode arrays (MEAs) to record the spontaneous action potentials (APs) fired by the neuronal network. These electrophysiological experiments revealed that the morphological maturation of the dendritic spines was accompanied by

increased synaptic activity. Indeed, over time and concomitant with morphological spine maturation, cultured MHNs acquired a spontaneous synchronized network-wide spiking activity that was evident after 12 DIV (Fig. S1A-E), as previously reported for *ex vivo* developing networks (Marom and Shahaf, 2002). Taken together, our morphological analysis and electrophysiology recordings, together with previous reports (Nwabuisi-Heath et al., 2012; Ziv and Smith, 1996), showed that dendritic spines of 14 DIV MHNs were undergoing progressive maturation.

SYNAPTOSOMAL FRACTIONATION

Post-synaptic density fractionations were prepared from brains obtained from 2 weeks old animals (mice or rats), as previously described (Cho et al., 1992), with inclusion of 10 μM of the proteasomal inhibitor MG132 in the lysis buffer.

PLASMIDS AND LENTIVIRAL VECTORS

The following plasmids were previously reported: pEYFP-N1 (Clontech), pcDNA3-myc-hFLNA-WT (Addgene #8640; transcript 1, NP_001447.2 (Woo et al., 2004)), p-sh-SCR and p-shPHD2 (Leite de Oliveira et al., 2012; Mazzone et al., 2009), pRSET-B-tdTomato (Shaner et al., 2004), 9xHRE::Luciferase (Aragones et al., 2001), pBrainbow1.0 (Livet et al., 2007), pOG231-NLS-Cre (O'Gorman et al., 1991), HA-VHL-pRc/CMV (Addgene #19999 (Iliopoulos et al., 1995)), pCAGGS-GFP (Niwa et al., 1991) and pCAGGS-RFP-11 (Attardo et al., 2008). Murine *Phd2* was cloned in frame in the pEYFP-N1 vector, to generate the $PHD2^{WT}$YFP fusion protein. The myc-tagged deletion mutants of hFLNA were generated by PCR from the pcDNA3-myc-hFLNA-WT plasmid. The TQ2-labeled full-length and C-terminus (2250-2639 aa.) of *hFLNA* were cloned in frame in the pTQ2-N1 plasmid (Goedhart et al., 2012). The $PHD2^{MUT}$YFP mutants (H290A/D292A (Vogel et al., 2010), $mycFLNA^{D21\text{-}D23\text{-}P2309A}$, $mycFLNA^{D21\text{-}D23\text{-}P2316A}$ and $mycFLNA^{D21\text{-}D23\text{-}3P\rightarrow A}$ (P2309/2312/2316A) were generated using the QuickChange mutagenesis kit (Stratagene). GST-fusion proteins were made by cloning the coding sequence of the *FLNA* fragments in the pGEX4-T2 plasmid (GE Healthcare). Lentiviral vectors were made using the pLVx-shRNA2 (scr, shPhd2, shPhd1, shFlna; Clontech), pLKO (scr, shVhl; Sigma) or pRRL (mycD21-D23) backbones.

LUCIFERASE ACTIVITY

Cells expressing Firefly luciferase were lysed and enzymatic luciferase activity was measured in a Microlumat LB96V Luminometer (Berthold Technologies).

IMMUNOBLOTS, IMMUNOPRECIPITATIONS AND PULL-DOWNS

For immunoblots, protein samples were separated by SDS-PAGE and transferred to 0.45-mm nitrocellulose membranes (Life Technologies). For immunoprecipitation, cells or tissue from mice or rats were lysed in chilled lysis buffer (50 mM Tris-HCl pH 7.5, 150 mM NaCl, 0.1% Triton-X100, 0.1% Brij35, 10% glycerol, 10 μM MG132 1% Complete protease inhibitor and 1% PhosSTOP (both from Roche)), and centrifuged at 15,000g for 10 min at 4ºC. Antibodies were pre-bound to protein A– or protein G–coated Dynabeads (Life Technologies) or agarose beads (Pierce or GE Healthcare). Lysates were incubated for 2 hrs-o/n at 4ºC. To isolate ubiquitinated proteins, samples were lysed in cold lysis buffer containing 10 μM PR-619 (Sigma), and centrifuged at 15,000g for 10 min at 4ºC. Lysates were incubated with agarose-TUBE2 (Life Sensors) for 16 h. *In vitro* binding assays were performed with GST-fusion proteins (expressed in *E. coli* BL21-Gold (DE3; Life Technologies)) and cell homogenates obtained from HEK293T cells transfected with YFP or $PHD2^{MUT}$YFP, and incubated for 2 h at 4ºC. GST complexes were pulled-down with glutathione-coated beads (GE Healthcare). For antibodies used in immunoblots, see below.

RNA ANALYSIS

IN SITU HYBRIDIZATION: In situ hybridizations (ISH) were made as previously reported (Ruiz de Almodovar et al., 2011), using DIG-labeled antisense probes for murine *Phd1 (Egln2)*, *Phd2 (Egln1)* or *Phd3 (Egln3)* or sense probes as control on PFA fixed cryosections or free-floating vibratome sections. *RT-PCR:* Cells were lysed and total RNA was isolated using the PureLink RNA Mini Kit (Life Technologies). Complementary DNA was synthetized by the QuantiTect Retrotranscriptase reaction (Qiagen). RNA expression analysis was performed by Taqman quantitative RT-PCR using in house-designed primers and probes or premade primer sets (IDT). Sequences or ID numbers are available upon request. *RNA-SEQ*: Brains of 2 weeks old mice were collected and total RNA was isolated using TRIZOL (Life technologies). Quantitative RNA-seq analysis (Illumina) was performed by the Genomics Core (KU Leuven-UZ Leuven).

IMMUNOHISTOCHEMISTRY

Immunohistochemical stainings were performed on 4% PFA fixed MHN or thick free-floating brain cryosections. Samples were permeabilized with PBS-0.1% Triton X-100, and blocked with 10% goat serum. Primary antibodies (see below) were incubated o/n at 4ºC. Secondary antibodies were Alexa-488, -568 -633 or -647 conjugated antibodies (Life Technologies). Slides were mounted with ProLong-Gold anti-fade mounting media containing DAPI (Life Technologies). Analysis of spines in vivo was made in 80-100 µm vibratome sections. Golgi staining was performed in 2 weeks old littermates, using the FD Rapid Golgi Stain Kit (FD NeuroTechnologies). TUNEL staining was performed in 4% PFA fixed MHN using the *In Situ* Cell Death Detection Kit (Roche).

ANTIBODIES

The following antibodies were used: rabbit anti-PHD2 (Novus); mouse anti-myc (9E10) and rabbit anti-FLNA (for IHC of rat FLNA) (Santa Cruz); rabbit anti-FLNA (for mouse FLNA in IB), rabbit anti-hydroxyprolines, rabbit anti-PSD-95 and rabbit anti-drebrin (Abcam); mouse anti-FLNA (for IP of rat FLNA), mouse anti-PSD-95 and guinea pig anti-vGlut1 (Millipore); mouse anti-GFP (JL8, Clontech); rabbit anti-GFP (Fitzgerald); mouse anti-α-tubulin and rabbit anti syntaxin (Sigma); rabbit anti-β-actin, rabbit anti-cleaved caspase 3, rabbit anti-pVHL and rabbit anti PTEN (Cell Signaling); mouse anti-synaptophysin and rabbit anti-ubiquitin (Dako); rat anti-HA (Roche); goat anti-HIF-1α (R&D Systems); rabbit anti-PARP1 (Enzo); rabbit anti-calretinin (Swant Inc.).

MASS SPECTROMETRY

IN GEL PROTEIN DIGESTION: Stained protein bands were excised from the gel, and in-gel tryptic digestion was performed as described previously (Wilm et al., 1996) with minor modifications. Briefly, after several washing steps (50 mM NH_4HCO_3 / 50% acetonitrile (ACN)) to eliminate the stain, the protein were reduced (10 mM DTT in 50 mM NH_4HCO_3 for 30 min at 56°C) and then alkylated (55 mM iodoacetamide in 50 mM NH_4HCO_3 for 30 min at room temperature in the dark). The gel pieces were washed in 50 mM NH_4HCO_3 and then dried in 100% ACN to be rehydrated in a sufficient covering volume of Trypsin solution (10 ng/µl in 10 mM NH_4HCO_3; Promega). Trypsin digestions were performed o/n at 37°C with shaking. Peptides were extracted once with 50 mM NH_4HCO_3, twice 5 % formic acid (FA) in 50% ACN and once with 100% ACN. The five extractions were combined and the mixture was dried down in a vacuum concentrator and then reconstituted in 12 µl H_2O/ACN/FA (98:2:0.1). *MASS SPECTROMETRY ANALYSIS, DATABASE SEARCH, AND PROTEIN IDENTIFICATION:* Digested peptides were analyzed by nano LC-MS/MS using an EASY-nLC 1000 (Thermo Fisher Scientific) coupled to a Q Exactive Orbitrap mass spectrometer. 5 µl of each sample were picked up at 300 nl/min, loaded on a home-made C_{18} 18 cm capillary column picotip silica emitter tip (75 µm diameter filled with 1.9 µm Reprosil-Pur Basic C_{18}-HD resin (Dr. Maisch GmbH, Ammerbuch-Entringen, Germany)) equilibrated in solvent A (0.1 % FA). The peptides were eluted using a 2 to 50 % two

slopes gradient of solvent B (0.1 % FA in ACN) during 47 min at 250 nl/min flow rate (total length of the chromatographic run was 80 min). The Q Exactive (Thermo Fisher Scientific) was operated in data-dependent acquisition mode with the XCalibur software (Thermo Fisher Scientific). Survey scan MS were acquired in the Orbitrap on the 300 – 1800 *m/z* range with the resolution set to a value of 70,000 at *m/z* = 400 in profile mode (AGC target at 1^E6). The 15 most intense ions per survey scan were selected for HCD fragmentation (NCE 28), and the resulting fragments were analyzed in the Orbitrap at 35,000 of resolution (m/z 400). Isolation of parent ion was set at 2.5 m/z and Underfill ratio at 2.5%. Dynamic exclusion was employed within 30 s. Data were searched using MaxQuant (1.4.1.2 version) (with the Andromeda search engine) against the human database from SwissProt and TrEMBL (Jan 21st 2014, 88,500 entries, of which 39,715 from SwissProt). The following search parameters were applied: Carbamidomethylation of cysteines was set as a fixed modification, and oxidation of methionine, protein N-terminal acetylation and Oxidation of Proline were set as variable modifications. The mass tolerances in MS and MS/MS were set to 10 ppm for each, respectively. Maximum peptide charge was set to 7 and 5 amino acids were required as minimum peptide length. Peptides and proteins identified with an FDR lower than 0.1% were considered as valid identification. For *GSSG/GSH MEASUREMENT*, lysates from 14 DIV control or treated MHNs were collected and the level of GSSG in percent of GSSG + GSH was determined using liquid chromatography-mass spectrometry. As positive control, MHN were treated with 100 μM H_2O_2 for 1 hr.

IN-UTERO ELECTROPORATION

Pregnant mice were isofluorane anaesthetized at E15.5 and laparotomy was performed to expose the uteri. Circa 2 μl of PBS containing 5 mg/ml of plasmid was injected into the lumen of the embryonic forebrain followed by electroporation of the hippocampal anlage using 8 pulses of 40 V, 50 ms each at 1 s interval delivered through platinum electrodes using a BTX-830 electroporator (Genetronics) as previously described (Pacary et al., 2012). Dendritic morphology of hippocampal CA1 neurons was investigated at P15. Briefly, mice were intracardially perfused with 4% PFA, and brains were removed and post-fixed for additional 24 h in 4% PFA. Brains were dissected and post-fixed in the same solution overnight at 4°C. Coronal brain sections (100 μm thick) were cut on a vibratome and mounted with Prolong antifade mounting media (Life Technologies) and imaged.

IMAGING AND TIME-LAPSE RECORDINGS

IMAGING was performed using a Zeiss LSM 510 Meta NLO, Zeiss LSM 780 confocal microscope (oil immersion objectives EC Plan-Neofluar 40x with NA 1.3, Plan-Apochromat 63x with NA 1.4, and alpha Plan-Apochromat 100x with NA 1.46) (Carl Zeiss) or Leica SP8x confocal microscope (Leica) (oil immersion objective 63x with NA 1.4). Bright field images were acquired with an Axioplan-2 microscope coupled to an Axiocam HRc (Carl Zeiss). For *TIME-LAPSE IMAGING UNDER NORMOXIA*, pictures were acquired every 5 min for 4 h at 37°C using a Zeiss LSM 780 confocal microscope. In the case of DMOG treatment, the movie started just when the drug was added on the culture media. For *TIME-LAPSE UNDER HYPOXIA*, cells were under 0.5% O_2, 5% CO_2 and 37ºC (GM230 Tri-Gas Mixer, CellASIC ® Onix Microfluidic Platform, Millipore) and images were captured every 5 min for 4 h at 37°C using a Zeiss LSM 510 Meta NLO. The movie just started when switching the cultures to hypoxic conditions. *SUPER-RESOLUTION IMAGING* was performed using a Zeiss Elyra Structured Illumination microscope (SR-SIM) (Carl Zeiss) equipped with an oil x63 Plan-Apochromat objective with NA 1.4, three SIM grid rotations and averaging 4 scans of each pixel. *FLIM-FRET:* Time-domain fluorescence lifetime imaging microscopy (FLIM) was performed in transiently transfected HEK293T cells grown on glass-bottom dishes and transfected with the indicated plasmids. FLIM data were obtained using a confocal laser-scanning Leica TCS SP5 microscope. A pulsed two-photon Titanium:sapphire laser (Mai Tai HP, Spectra Physics, Newport) tuned at 820 nm was used for excitation. The excitation light was directed to the sample through a 63x (NA 1.2) water immersion objective. The emission light was filtered using a short pass 665 nm filter and a BP480/40 nm band pass filter. Finally, an APD detector (H7429-40,

Hamamatsu) connected to PicoQuant TCSPC hardware (PicoQuant) was used to detect the emission light, allowing for time-correlated single photon counting. FLIM images were processed using SymPhoTime software (PicoQuant). The quality of the fit was judged by the reduced χ^2–values. For the majority of the pixels the reduced χ^2–value was smaller than 1.2. *GOLGI IMPREGNATION:* To detect the Golgi impregnation, the Zeiss LSM780 confocal microscope was automatically set up in reflection mode by using a 488 nm wavelength and replacing the dichroic filter by a 20/80 beam splitter (Spiga et al., 2011). Images were acquired with an alpha Plan-Apochromat 100x/1.46 oil objective. No barrier filter was used to direct the reflected light by the sample to the detector. *ELECTRON MICROSCOPY* was performed using a JEM-1400 transmission electron microscope (Jeol, Zaventem, Belgium), equipped with an 11Mpixel Olympus SIS Quemesa camera. Ctrl and $PHD2^{NKO}$ littermates were processed as previously described (Arranz et al., 2015). Briefly, mice (N=3-4 mice) were transcardially perfused with 2.5% glutaraldehyde, 2% paraformaldehyde in 0.1 M cacodylate buffer. Brains were dissected and post-fixed in the same solution overnight at 4°C. Coronal brain sections (300 µm thick) were cut on a vibratome and rectangular pieces of tissue comprising the *striatum* were dissected. Tissue was post-fixed with 1% OsO_4, 1.5% $K_4Fe(CN)_6$ in 0.1 M cacodylate buffer, rinsed, stained with 3% uranyl acetate and dehydrated in graded ethanols and propyleneoxide, followed by embedding in EMbed812. Ultrathin sections (70nm) were obtained using an ultramicrotome (Leica Reichert Jung Ultracut E), mounted on 400 mesh copper grids and contrasted with uranyl acetate and lead citrate before being imaged. Images were taken at 2500X magnification.

MORPHOMETRIC ANALYSIS AND QUANTIFICATIONS

MORPHOMETRIC ANALYSIS AND QUANTIFICATIONS were done in primary and secondary dendrites, and the protrusions included in these dendrites. Synaptic density was assessed as previously described (Segura et al., 2007). Quantifications were done with NIH ImageJ software, using neurons from 3 independent experiments (isolations), with $n \geq 7$ neurons per condition/experiment, unless otherwise stated. All quantifications and manual counting were performed by persons, blinded for the experimental conditions. *QUANTIFICATION OF PROTRUSION LENGTH IN TIME-LAPSE MOVIES* was determined as follows. We measured the length of the spines, at the starting point and after different time points. Spines with variations ≤0.2 µm were considered stable. All imaged spines were measured at the starting point (0 hrs) and end (1 hr for hypoxia or 4 hrs for DMOG and shPHD2) of the time-lapse imaging (Fig. 1G,O; Fig. 3O). For the quantifications monitored over time at different time intervals using control or DMOG-treated neurons (Fig. S2A), we selected spines that were ≤2 µm long at the start of the analysis (≈75-80% of the spines were ≤2 µm in both cases), since this is the length of mature spines in the hippocampus (Sorra and Harris, 2000). We then followed over time how these spines responded to control vehicle or DMOG treatment. To evaluate the effect of PHD2 silencing, MHNs were transfected at 7 DIV with scr or shPHD2 constructs, and evaluated at 7 days later. Spines showed differences in length (spines >2 µm: ≈25% for scr vs. ≈70% for shPHD2), and they were randomly selected for quantification (Fig. S3K). *SYNAPTIC DENSITY IN VIVO* was determined by measuring the fluorescent signal detected per area unit of the *stratum radiatum* of the CA1 hippocampal region. The same threshold was set for all the images. *QUANTIFICATION OF SYNAPTIC DENSITY IN VITRO* was determined as previously reported (Hotulainen et al., 2009; Kayser et al., 2008; Segura et al., 2007). Briefly, to identify single dendrites, we transfected MHN at 14 DIV either with YFP (green) or tdTomato (tdT; red) fluorescent proteins, and performed the staining at 21 DIV. We performed two different stainings: (I) anti-vGlut and anti-PSD-95 co-staining or (II) anti-synaptophysin staining. In the first case, we counted the number of $vGlut^+/PSD\text{-}95^+$ co-clusters that were localized on the fluorescently labeled dendrite. In the second case, for every single dendrite analyzed, we counted only those synaptophysin-positive clusters, (i) in which immunoreactive signal completely colocalized with the positive signal of the dendrite to yield a yellow cluster, or (ii) in which the immunoreactive signal was in immediate close apposition with ("touching") the positive signal of a dendrite or its spines, when analyzed with a 63-fold magnification. Under those conditions, the distance between the "touching" (red or green) signals was <200nm. *GENERAL NOTE:* In all panels showing immunostaining of neuronal cultures for vGlut1, synaptophysin, PSD95, PHD2 or FLNA, immunoreactive signals are not only confined to the contours of the neuron under

investigation (transfected with a fluorescent reporter to reveal its dendritic protrusions), but are also detectable as positive stainings in neighbouring neurons, which themselves are however not transfected with a fluorescent reporter and therefore their cell body is not visible in the image. High-density cultures had to be used to allow maintenance of the neuronal cultures for prolonged periods; transfection with fluorescent reporters (see above) was done using conditions transfecting only a fraction of the neurons to allow visualization of single neurons.

CELLULAR AND NETWORK ELECTROPHYSIOLOGY

Patch-clamp recordings of the membrane electrical potential of cultured hippocampal neurons were performed at 14 and 21 days after plating, as described (Reinartz et al., 2014) from the cell somata, under the whole-cell configuration using an Axon Multiclamp 700B Amplifier (Molecular Devices LLC, Sunnyvale, CA, USA), in current-clamp mode. Overnight hypoxic treatment or incubations with DMOG (250 μM) were performed the day prior the recordings. Patch electrodes were pulled from standard borosilicate glass (1B150F-4, World Precision Instruments, Sarasota, FL, USA) by a horizontal puller (P97, Sutter, Novato, CA, USA) to a resistance of 6-7MΩ. Electrodes were filled with an intracellular solution containing (in mM): 135 K-gluconate, 10 KCl, 10 HEPES, 0.2 EGTA, 4 Mg-ATP, 0.4 Na_3GTP, and 14 Na_2-phosphocreatine (pH 7.3, titrated with KOH). All recordings were obtained at 34°C shortly after replacing the culture medium by an artificial cerebro-spinal fluid, constantly perfused at a rate of 1ml/min and containing (in mM): 145 NaCl, 4 KCl, 2 Na-pyruvate, 5 HEPES, 5 glucose, 2 $CaCl_2$, and 1 $MgCl_2$ (pH adjusted to 7.4 with NaOH). Voltage traces were sampled at 20 kHz, A/D converted at 16 bits, and stored on a personal computer employing the software LCG (Linaro et al., 2014). The same hardware/software system was employed to synthesize a variety of current-clamp stimulation waveforms, employed for estimating passive (i.e., membrane capacitance and input resistance) and active neuronal properties (i.e., rheobase current, frequency-current curve, spike-frequency adaptation index) of single cells. Recordings were analyzed off-line, employing custom scripts written in MATLAB (The MathWorks, Natick, US) or Excel (Microsoft, USA). The minor differences in AP's trajectory features (Fig. 2H, S3G) reflect the impact of hypoxia or DMOG on cell excitability (not significant).

Network-level extracellular recordings were performed in Neurobasal medium, supplemented with 1x B27 and 0.5 mM glutamine (Life Technologies). Across five distinct dissociation procedures, sister and non-sister cultures were plated on 28 MEAs. Hypoxic incubation was made in 1% O_2, 5% CO_2, and 94% N_2 atmosphere. The DMOG treatment was performed by adding it to the MEAs' bath at 1 mM final concentration. The described experiments were made overnight between DIV 13-14 and 20-21. Lentiviral transduction was accomplished by incubating overnight the neurons with 10 MOI particles. The electric network activity was recorded on all MEAs at DIV 13,14,15, and from DIV 20 to 22 only for hypoxia experiments. Electrophysiological recordings were performed by means MEA1060BC amplifiers, (Multichannel Systems GmBH, Reutlingen, Germany) inside an electronic friendly incubator, maintaining 37°C, 5% CO2, and 100% R.H. This allowed us to monitor simultaneously, chronically, and non-invasively the neuronal electrical activity from up to 59 locations within the very same culture. MEA recordings were analyzed off-line by QSpikeTools (Mahmud et al., 2014). Briefly, the extracellular electric fields were monitored from up to 59 independent electrodes in each MEAs, sampled at 25 kHz / channel, 1200x amplified, bandpass-filtered (400-3000Hz), and digitally recorded for 60 min every day. Elementary spike-sorting, only based on spike-shape peak polarity, was performed. Epochs of spontaneous synchronized firing across the MEAs electrodes were identified over 1 ms bins and by employing a threshold equal to 10. Neurons excitability in all MEAs was probed by low frequency (0.2 Hz) electrical extracellular stimulation, employing a stimulus isolator (STG1002, Multichannel Systems, Germany) programmed and driven by a custom made MATLAB (The MathWorks, USA). Four electrodes were chosen after probing 10 random sites of all electrodes. Stimuli were characterized by a square biphasic waveform of 1 ms duration and 1.6 V amplitude.

SUPPLEMENTAL REFERENCES

Aragones, J., Jones, D.R., Martin, S., San Juan, M.A., Alfranca, A., Vidal, F., Vara, A., Merida, I., and Landazuri, M.O. (2001). Evidence for the involvement of diacylglycerol kinase in the activation of hypoxia-inducible transcription factor 1 by low oxygen tension. J Biol Chem *276*, 10548-10555.

Arranz, A.M., Delbroek, L., Van Kolen, K., Guimaraes, M.R., Mandemakers, W., Daneels, G., Matta, S., Calafate, S., Shaban, H., Baatsen, P.*, et al.* (2015). LRRK2 functions in synaptic vesicle endocytosis through a kinase-dependent mechanism. J Cell Sci *128*, 541-552.

Attardo, A., Calegari, F., Haubensak, W., Wilsch-Brauninger, M., and Huttner, W.B. (2008). Live imaging at the onset of cortical neurogenesis reveals differential appearance of the neuronal phenotype in apical versus basal progenitor progeny. PLoS One *3*, e2388.

Goedhart, J., von Stetten, D., Noirclerc-Savoye, M., Lelimousin, M., Joosen, L., Hink, M.A., van Weeren, L., Gadella, T.W., Jr., and Royant, A. (2012). Structure-guided evolution of cyan fluorescent proteins towards a quantum yield of 93%. Nat Commun *3*, 751.

Haase, V.H., Glickman, J.N., Socolovsky, M., and Jaenisch, R. (2001). Vascular tumors in livers with targeted inactivation of the von Hippel-Lindau tumor suppressor. Proceedings of the National Academy of Sciences of the United States of America *98*, 1583-1588.

Hotulainen, P., Llano, O., Smirnov, S., Tanhuanpaa, K., Faix, J., Rivera, C., and Lappalainen, P. (2009). Defining mechanisms of actin polymerization and depolymerization during dendritic spine morphogenesis. J Cell Biol *185*, 323-339.

Iliopoulos, O., Kibel, A., Gray, S., and Kaelin, W.G., Jr. (1995). Tumour suppression by the human von Hippel-Lindau gene product. Nat Med *1*, 822-826.

Kayser, M.S., Nolt, M.J., and Dalva, M.B. (2008). EphB receptors couple dendritic filopodia motility to synapse formation. Neuron *59*, 56-69.

Leite de Oliveira, R., Deschoemaeker, S., Henze, A.T., Debackere, K., Finisguerra, V., Takeda, Y., Roncal, C., Dettori, D., Tack, E., Jonsson, Y.*, et al.* (2012). Gene-targeting of Phd2 improves tumor response to chemotherapy and prevents side-toxicity. Cancer cell *22*, 263-277.

Linaro, D., Couto, J., and Giugliano, M. (2014). Command-line cellular electrophysiology for conventional and real-time closed-loop experiments. J Neurosci Methods *230*, 5-19.

Livet, J., Weissman, T.A., Kang, H., Draft, R.W., Lu, J., Bennis, R.A., Sanes, J.R., and Lichtman, J.W. (2007). Transgenic strategies for combinatorial expression of fluorescent proteins in the nervous system. Nature *450*, 56-62.

Mahmud, M., Pulizzi, R., Vasilaki, E., and Giugliano, M. (2014). QSpike tools: a generic framework for parallel batch preprocessing of extracellular neuronal signals recorded by substrate microelectrode arrays. Front Neuroinform *8*, 26.

Marom, S., and Shahaf, G. (2002). Development, learning and memory in large random networks of cortical neurons: lessons beyond anatomy. Q Rev Biophys *35*, 63-87.

Niwa, H., Yamamura, K., and Miyazaki, J. (1991). Efficient selection for high-expression transfectants with a novel eukaryotic vector. Gene *108*, 193-199.

O'Gorman, S., Fox, D.T., and Wahl, G.M. (1991). Recombinase-mediated gene activation and site-specific integration in mammalian cells. Science *251*, 1351-1355.

Ruiz de Almodovar, C., Fabre, P.J., Knevels, E., Coulon, C., Segura, I., Haddick, P.C., Aerts, L., Delattin, N., Strasser, G., Oh, W.J*., et al.* (2011). VEGF mediates commissural axon chemoattraction through its receptor Flk1. Neuron *70*, 966-978.

Ryan, H.E., Poloni, M., McNulty, W., Elson, D., Gassmann, M., Arbeit, J.M., and Johnson, R.S. (2000). Hypoxia-inducible factor-1alpha is a positive factor in solid tumor growth. Cancer Res *60*, 4010-4015.

Shaner, N.C., Campbell, R.E., Steinbach, P.A., Giepmans, B.N., Palmer, A.E., and Tsien, R.Y. (2004). Improved monomeric red, orange and yellow fluorescent proteins derived from Discosoma sp. red fluorescent protein. Nat Biotechnol *22*, 1567-1572.

Sorra, K.E., and Harris, K.M. (2000). Overview on the structure, composition, function, development, and plasticity of hippocampal dendritic spines. Hippocampus *10*, 501-511.

Spiga, S., Acquas, E., Puddu, M.C., Mulas, G., Lintas, A., and Diana, M. (2011). Simultaneous Golgi-Cox and immunofluorescence using confocal microscopy. Brain Struct Funct *216*, 171-182.

Tronche, F., Kellendonk, C., Kretz, O., Gass, P., Anlag, K., Orban, P.C., Bock, R., Klein, R., and Schutz, G. (1999). Disruption of the glucocorticoid receptor gene in the nervous system results in reduced anxiety. Nature genetics *23*, 99-103.

Wilm, M., Shevchenko, A., Houthaeve, T., Breit, S., Schweigerer, L., Fotsis, T., and Mann, M. (1996). Femtomole sequencing of proteins from polyacrylamide gels by nano-electrospray mass spectrometry. Nature *379*, 466-469.

Woo, M.S., Ohta, Y., Rabinovitz, I., Stossel, T.P., and Blenis, J. (2004). Ribosomal S6 kinase (RSK) regulates phosphorylation of filamin A on an important regulatory site. Molecular and cellular biology *24*, 3025-3035.

Ziv, N.E., and Smith, S.J. (1996). Evidence for a role of dendritic filopodia in synaptogenesis and spine formation. Neuron *17*, 91-102.

INVENTORY OF SUPPLEMENTAL INFORMATION

Supplemental Figures

Figure S1; related to Figure 1

Figure S2; related to Figure 1

Figure S3; related to Figure 2

Figure S4; related to Figure 3

Figure S5; related to Figure 3

Figure S6; related to Figure 3

Figure S7; related to Figure 4

Figure S8; related to Figure 5

Figure S9; related to Figure 6

Supplemental Experimental Procedures

Supplemental References